Temporal velocity variations in the northern Hikurangi margin and the relation to slow slip

Weiwei Wang[1,2], Martha K. Savage[1], Alexander Yates[1,3], Hubert J. Zal[1], Spahr Webb[4], Carolyn Boulton[1], Emily Warren-Smith[5], Megan Madley[1,5], Tim Stern[1], Bill Fry[5], Kimihiro Mochizuki[6], Laura Wallace[5,7]

[1]Victoria University of Wellington, Wellington, New Zealand
[2]The University of Auckland, Auckland, New Zealand
[3]Université Grenoble Alpes, Université Savoie Mont Blanc, CNRS, IRD, IFSTTAR, ISTerre, 38000 Grenoble, France
[4]Lamont-Doherty Earth Observatory, Columbia University, Palisades, NY, USA
[5]GNS Science, Lower Hutt, New Zealand
[6]Earthquake Research Institute, University of Tokyo, Tokyo, Japan
[7]University of Texas Institute for Geophysics, Austin, TX, USA

Keywords: slow slip event, the Hikurangi subduction zone, ambient noise, seismic velocity variations

Corresponding author: Weiwei Wang, `weiwei.wang204@hotmail.com`

Abstract

Slow slip events (SSE) have been studied in increasing detail over the last 20 years, improving our understanding of subduction zone processes. Although the relationship between SSEs and the physical properties of their surrounding materials is still not well-understood, the northern Hikurangi margin in New Zealand is the site of relatively shallow (<10 km deep), frequent SSEs, providing excellent opportunities for near-field investigations. From September to October 2014, an SSE occurred with more than 250 mm slip, and was recorded successfully by the Hikurangi Ocean Bottom Investigation of Tremor and Slow Slip (HOBITSS) deployment. This study applies scattered wave interferometry to ambient noise data acquired by nine HOBITSS ocean bottom seismometers (OBS) to study the seismic velocity variations related to the SSE. Single station cross-component correlations are computed within a period band that focuses on the upper plate in our study region. The average velocity variations display a decrease on the order of 0.05% during the SSE, followed by an increase of similar magnitude afterwards. We suggest two possibilities. The first possibility, which has been suggested by other seismological observations, is that the SSE causes a low-permeability seal on the plate boundary to break. The break allows fluid to migrate into the upper plate, causing a seismic velocity decrease during the SSE because of increased pore fluid volume in the upper plate. Under this model, after the SSE, the fluids in the upper plate diffuse gradually and the velocity increases again. The second possibility is the velocity changes are related to changes in crustal strain during the slow slip cycle, whereby elastic strain accumulates prior to the SSE, causing contraction and reduction of porosity and therefore increase of velocity above the SSE source (the seismic velocity increases between SSEs). During the SSE the upper plate goes into extension as the elastic strain is released, which results in dilation and a porosity increase (seismic velocity reduction). After the SSE, stress and strain accumulate again, causing a porosity decrease and a velocity increase.

Highlights

- Seismic velocity decreases during a Hikurangi margin SSE and increases after
- Interpretation 1: Fluids migrate to upper plate during the SSE and diffuse after
- Interpretation 2: Porosity increases during the SSE and decreases after

1 Introduction

Slow slip events (SSEs), involving fault slip over days to years, have been a topical field of tectonics and fault mechanics research as they extend our understanding of subduction zone deformation. The occurrence of SSEs, and how it relates to the physical properties of surrounding materials, remains an outstanding question, although geophysical observations from subduction zones globally are helping to constrain this relationship. *Schwartz and Rokosky* (2007) reviewed SSEs on circum-Pacific subduction zones and indicated slow slip occurs in most subduction zones. They suggested that fast and slow slip are likely controlled by different frictional properties. *Ito et al.* (2013) discovered that SSEs in 2008 and 2011 occurred on the same portions of the megathrust fault as the 2011 Tohoku-Oki earthquake, suggesting that areas holding SSEs can also rupture seismically. *Nakajima and Uchida* (2018) found variations in seismicity rates and seismic attenuation with the cyclic occurrence of SSEs in Kanto, Japan, which they interpreted to represent intensive drainage during SSEs. *Gosselin et al.* (2020) observed a seismic velocity change after episodic tremor and SSEs in Cascadia, which they interpreted to reflect fluctuations in pore fluid pressure.

The Pacific Plate subducts beneath the Australian Plate along the Hikurangi margin. The Hikurangi margin can be divided into three segments (Figure 1 inset): northern, central and southern. Shallow SSEs occur in the northern and central segments, while deep SSEs (>25-30 km depth) are observed in the southern segment (*Wallace and Beavan*, 2010). In the northern Hikurangi margin, the plate interface is 10-15 km deep, enabling identification of shallow (<10 km) SSEs using land-based geophysical networks (e.g., *Wallace and Beavan*, 2010). The equivalent plate interfaces at many other subduction zones are >50-100 km offshore, making them difficult to study SSEs.

The northern Hikurangi is the site of some of the world's shallowest, well-documented SSEs. SSEs have been observed there since continuous GNSS were installed in 2002 (e.g., *Wallace and Beavan*, 2010). SSEs offshore Gisborne occur approximately every 1-2 years, and are detected by continuously operating GNSS sites near the coast. To provide improved resolution of SSE processes on the offshore plate boundary, the HOBITSS project deployed 24 absolute pressure gauges and 15 ocean bottom seismometers (OBSs) from mid-2014 to mid-2015. Four SSEs occurred during this deployment (SSE1-SSE4); the locations of these SSEs are shown in Figure 1 and Figure S1. *Warren-Smith et al.* (2019) calculate the timing of these SSEs from time-dependent geodetic inversions. SSE1 occurred to the south of the deployment region from 1st September to 17th November 2014. SSE2 occurred from 24th September to 2nd November 2014 directly beneath the HOBITSS network. SSE3 occurred from 18th December 2014 to 12th January 2015. The main slip of SSE3 occurred mostly south of the HOBITSS deployment but also within a part of the HOBITSS deployment region. SSE4 occurred from 7th February to 1st March 2015 outside of the deployment region. We focus primarily on SSE2, which recorded the largest slip, equivalent to a moment magnitude of Mw 6.8. The main pulse of slip from late September to mid-October, with a tailing off period from mid to late October (*Wallace et al.*, 2016; *Warren-Smith et al.*, 2019). The largest slip (> 200 mm) occurred at a depth of 4-7 km beneath the central portion of the HOBITSS network (*Wallace et al.*, 2016).

In subduction zones, increased pore fluid pressure due to mineral dehydration and compaction likely influences the mechanism of earthquakes and SSEs (*Saffer and Tobin*, 2011; *Chaves and Schwartz*, 2016). *Warren-Smith et al.* (2019) calculated earthquake focal mechanisms of local microseismicity using the data recorded by the HOBITSS deployment to determine the stress ratio variations within the subducting oceanic crust during the SSE cycle. The stress ratio $R_{retr} = (\sigma_1 - \sigma_2)/(\sigma_1 - \sigma_3)$ is retrieved from focal mechanism inversion, where σ_1, σ_2 and σ_3 are the maximum, intermediate and minimum principal stresses respectively. Because the Pacific plate is subducting at a shallow angle, σ_1 is nearly perpendicular to the interface and σ_3 is oriented down-dip and aligned with tensional slab pull. Pore fluid pressure has a negative correlation to the retrieved stress ratio (*Martínez-Garzón et al.*, 2016). Observations by *Warren-Smith et al.* (2019) showed that the stress ratio in the lower plate decreased before SSE2 and increased during SSE2, suggesting pore fluid pressure increased in the lead-up to SSE2, and then decreased during SSE2, and similar patterns occurred during the other three SSEs observed during HOBITSS. This is interpreted as increased fluid pressurization below a low-permeability barrier prior to slow slip, and subsequent fluid migration arising from increased strain induced permeability during SSEs. *Zal et al.* (2020) use local earthquakes with seismic ray paths largely traveling through the upper plate to compute shear wave splitting and Vp/Vs ratios at the HOBITSS OBS sites. They find the Vp/Vs ratios increase and shear wave splitting delay times decrease during SSE2, implying the amount of fluid in the upper plate increases during SSE2. Their studies suggest fluid accumulation and release before and during SSE2 as SSE2 breaks the permeability seal on the plate boundary and permits the required fluid interconnection, which is broadly consistent with the observations and model of *Warren-Smith et al.* (2019).

Seismic velocities computed using ambient noise interferometry have been used in the last fifteen years to monitor changes in subsurface material properties, including those caused by large earthquakes (e.g., *Brenguier et al.*, 2008). *Rivet et al.* (2011) use this method to study an SSE in Mexico in 2006 with a size equivalent to an M7.5 earthquake. They observe a velocity decrease in the upper and middle crust during the SSE and suggest it is related to the strain rate, suggesting the overlying crustal deformation shows nonlinear elastic behavior during the SSE. For the same SSE, *Frank et al.* (2015) suggest that fluids play an active role in SSE source; they interpret variations of rates of low frequency earthquakes as caused by a pore pressure fluctuation that migrates updip along the subduction interface. In the same subduction zone, *Rivet et al.* (2014) studied velocity changes, strain rate and non-volcanic tremors during a 2009–2010 SSE. Their study supported the finding of *Rivet et al.* (2011) and suggested that velocity changes are related to tremor activity in the period range for which velocity variations produced by the SSE are identified.

Additional techniques that help to constrain the timescales and magnitudes of stress and fluid pressure variability in SSEs are required to complement previous methodologies. This paper uses ambient noise data recorded by the HOBITSS instruments to compute seismic velocity changes and to examine implications for changes in physical properties of the crust through the SSE cycle.

2 Data

From May 2014 to June 2015, the HOBITSS project deployed ten broadband OBSs from Lamont Doherty Earth Observatory (LOBS) with a velocity response flat down to 100 s, and five short period OBSs from Earthquake Research Institute, Japan (EOBS) with a natural period of 1 s, offshore from

Published in *EPSL; DOI: 10.1016/j.epsl.2022.117443*

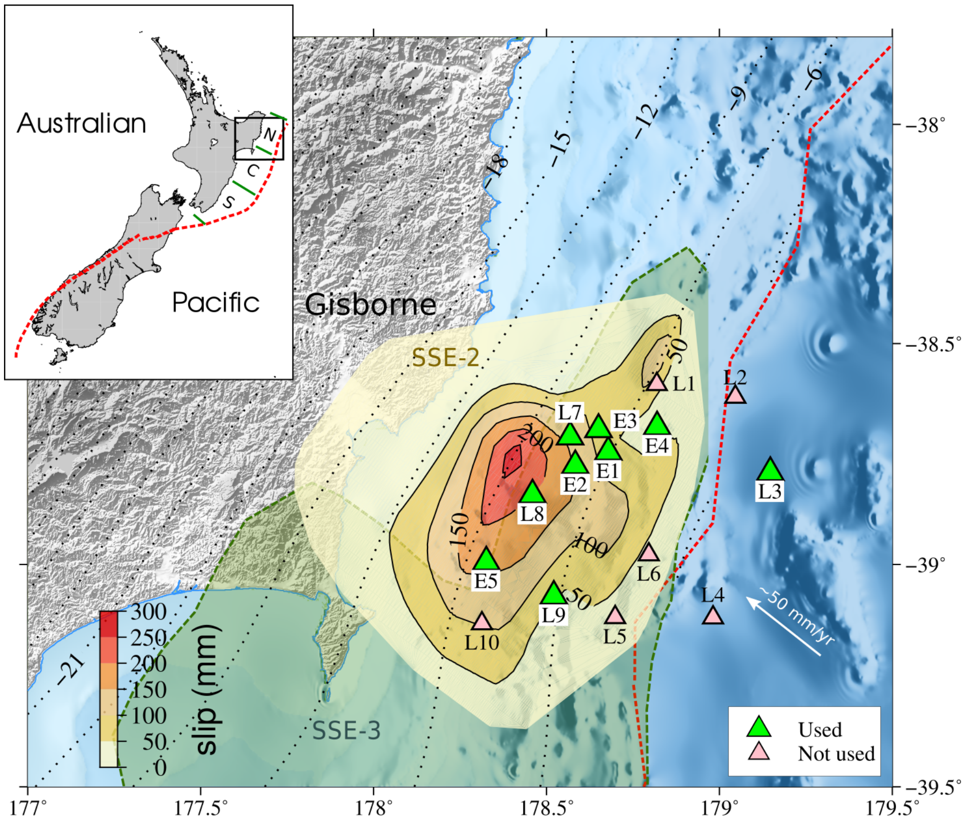

Figure 1. Locations of ocean bottom seismometers (OBSs; *TAN1405 Science Party*, 2014) with the contours showing the slip from SSE2 occurring from September to October 2014 (*Wallace et al.*, 2016). The green shade shows the location of SSE3, which is shown in full in the map in supplementary Figure S1. Station names are shortened from LOBS to L and EOBS to E. The green triangles denote the stations used in this study and the pink stations are not used. The dashed red line shows the subduction trench (*Coffin et al.*, 1998) and black dotted contours show the plate interface depth in km (*Williams et al.*, 2013). Global Earth Relief Grids 15 s is used for the bathymetry (*Wessel et al.*, 2013). The three segments N (northern), C (central), and S (southern) of the Hikurangi margin are indicated in the inset.

Gisborne (Figure 1). Three stations, LOBS2, LOBS3, and LOBS4 were deployed on the subducting Pacific Plate as reference sites, while the remaining stations were deployed on the overlying Australian plate to record signals associated with the underlying slow slip region.

Continuous data recorded by nine OBSs (green triangles in Figure 1) are used to compute single station cross component correlation functions. Stations LOBS1, LOBS2, LOBS4, LOBS5, and LOBS10 did not acquire sufficient data and are not used in our analysis. The orientations of LOBS6 horizontal components could not be determined (*Zal et al.*, 2020) and so LOBS6 is not used in this study. Cross-station correlations are not included in this study because of instrument timing issues (see supplemental material in *Yarce et al.* (2019)), which do not influence single station correlations.

Horizontal station components are rotated to be parallel and perpendicular to the coastline according to the orientations determined by P waves and Rayleigh waves of teleseismic events (*Zal et al.*, 2020). Scattered waves are derived from single station vertical-parallel cross correlations, vertical-perpendicular cross-correlations, and parallel-perpendicular cross-correlations.

3 Methods

Velocity variations are determined using scattered waves retrieved from single station cross component correlations, which represent the waves traveling out from the station and back at later time. Seismic noise data are processed through to velocity changes using a Python package MSNoise 1.5 (*Lecocq et al.*, 2014). Parameters in MSNoise are tested, evaluated, and determined, with the aim of maximizing the lag-time dependent signal-to-noise ratio (SNR; *Larose et al.*, 2007; *Clarke et al.*, 2011) of cross-correlation functions (e.g., *Yates*, 2018). The coherence and correlation coefficient between current stacks and reference stacks are calculated to evaluate data quality (Supporting Information S1). The final parameters are listed in Table S1.

Each station is processed independently. Three-component daily noise records of each station are band pass filtered from 0.5 to 50 s and down sampled to 20 Hz. Time domain normalization is applied through clipping data at three times the Root-Mean-Square as in previous studies (*Lecocq et al.*, 2014; *Yates et al.*, 2019), followed by spectral whitening between 2.5 to 20 s (Figure S2). Different multipliers (1, 3, 5) for Root-Mean-Square clipping are tested, with no measurable differences in our results. Daily series are cut to 14400 s segments for LOBSs and 1800 s segments for EOBs, with 70% overlap in window length, to correlate, because these segment lengths lead to higher SNR than other lengths (Figure S3). The cross-correlations are then linearly stacked to give daily cross-correlations. Correlation coefficients between these and the stack of all days for a single station are computed, and daily cross-correlations are excluded if they fall below a threshold (e.g., Figure S4). The threshold varies from station to station (0.1 to 0.65), to guarantee a sufficient number of daily cross-correlations for velocity change computation, while discarding the lowest quality cross-correlations for each station. The correlation coefficients are generally low because OBSs have higher noise levels than land stations. The daily cross-correlations after selection are re-stacked as a reference. Figure S5 shows the final available cross-correlations of all the used stations and Figure S6 shows the reference stacks.

Velocity changes are determined by measuring the delay time (dt) between smaller 'current' stacks and a reference stack over different lag times (t). A velocity change is then computed by fitting a slope to delay times computed using the moving-window cross-spectral approach (*Clarke et al.*, 2011; *Poupinet et al.*, 1984) where, under the assumption of a homogeneous velocity change, we have $-dt/t = dv/v$, with dv/v the fractional velocity change. The reference stack ideally represents the background state of the study region. Current stacks should be similar to the reference stack, where it is often necessary to stack multiple daily cross-correlations to average out incoherent noise at the cost of temporal resolution. Multiple references stacks are tested, including a linear stack of all available days and stacks using only daily stacks prior to SSE1 and SSE2 (Figure S7). We observe similar velocity variations regardless of the choice of reference stack and opt to use the reference stack of all available days. Current stacks are chosen to be linear stacks of 20 daily cross-correlation functions (Figure S4). This stacking improves the SNR of the scattered wave energy by suppressing random noise. The current stack for a given date represents the stack of that day and 19 days before it. As a consequence, we are limited in our ability to distinguish between a gradual velocity change over 20-days and one occurring over a much shorter time period. Figure 2 shows an example of the current stacks and the reference stack from one station.

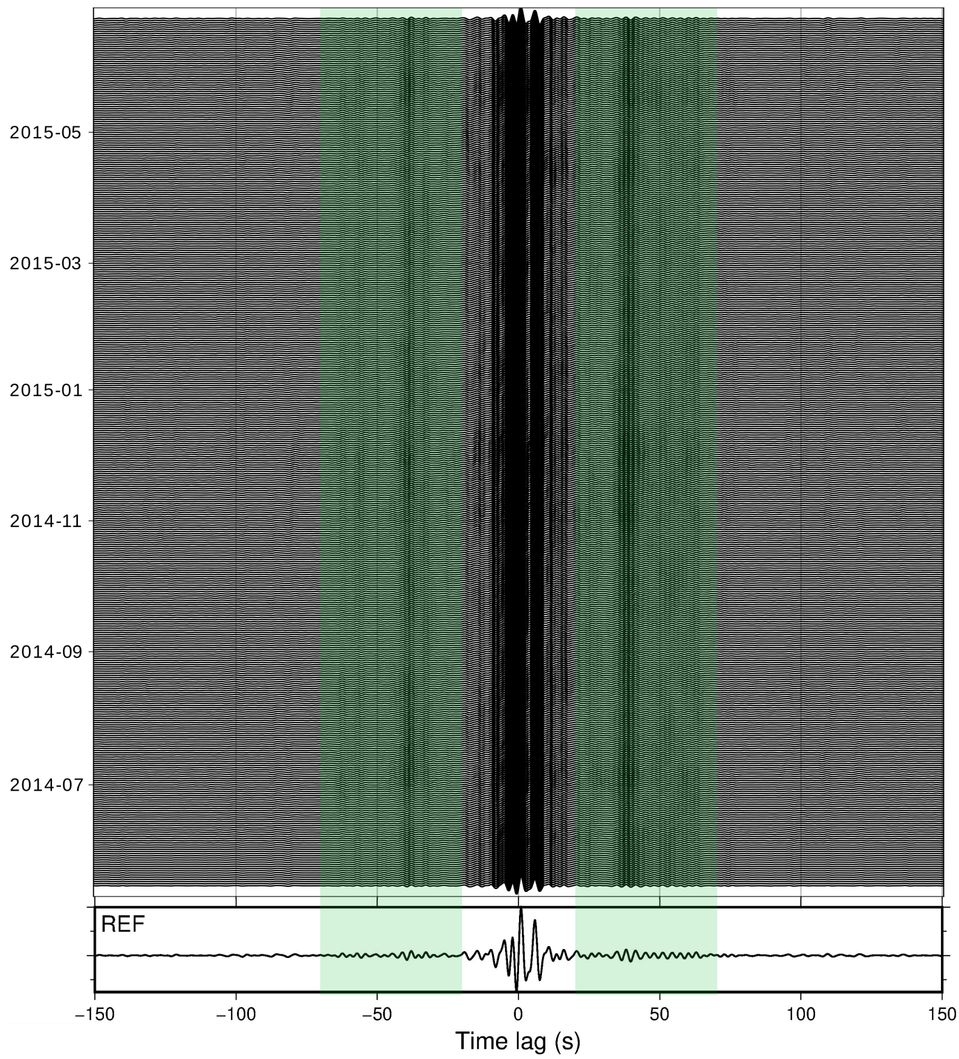

Figure 2. 20-day current stacks over time from EOBS1 vertical-perpendicular component correlations and corresponding reference stack. The green shades mark the window (-70 s to -20 s and 20 s to 70 s) to compute velocity variations.

Delay times between current and reference stacks are measured using the moving-window cross-spectral approach (*Clarke et al.*, 2011; *Poupinet et al.*, 1984). Specifically, the delay time between the current and reference function is obtained in a series of moving windows. For this study, we use 20-second moving windows with a 4-second step (80% overlap). The final velocity change is then computed using delay time measurements within a lag time window ±20 s to ±70 s. This window has higher SNR, suggesting the presence of coherent scattered wave energy (Supporting Information S1). Certain quality control criteria are applied to ensure only delay time measurements of sufficient quality are included in the computation of velocity changes. The coherence between a current stack and the reference stack is computed and a threshold of coherence is set to 0.89 to exclude poor current stacks (Figure S8). Delay time measurements greater than 0.2 seconds or with an error greater than 0.1 seconds are excluded. A frequency band of 2.5-14 s is used when applying the moving-window cross-spectral analysis method. In our study, surface waves with periods up to 14 s are most sensitive to properties of the upper plate (Figures 3 and 4). The first overtone mode is considered because observations of seafloor ambient noise show a transition from most of the noise energy in the fundamental mode at long periods to the first overtone mode at shorter period (< 6 s; *Harmon et al.*, 2007; *Russell et al.*, 2019). The EOBSs are short-period instruments with a natural period of 1 s. Spectral analyses within the scattered wave window of the reference stacks (Figure S9) show, for most stations, the scattered waves are dominant at 2.5-6 s. As in Figure S10, the dv/v at 2.5-14 s is similar to the dv/v at 2.5-6 s, but we can still see similar velocity changes at longer periods (6-14 s; Figure S11). Possibly there are signals at longer periods (6-14 s), but if so, they are weaker compared to short periods (2.5-6 s). This does not affect our focus on depth, because there is little difference in depth sensitivity kernels between 2.5-6 s and 2.5-14 s (Figures 3 and 4). Therefore, below we present the results of 2.5-14 s.

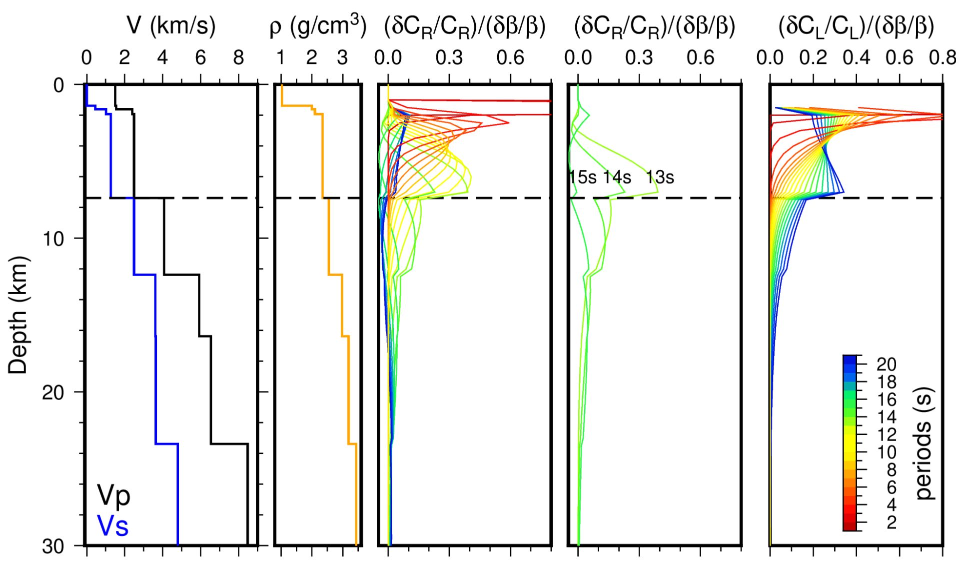

Figure 3. Velocity and density models in the study region and corresponding sensitivity kernels of fundamental mode Rayleigh wave phase velocities (C_R) and fundamental mode Love wave phase velocities (C_L), with respect to shear wave velocities (β). The sensitivity kernels are color-coded according to corresponding periods. Velocity models are from *Yarce et al.* (2019), combined with the information of Vp and Vs from ODP U1519. The density model is from New Zealand Wide model 2.2 (*Eberhart-Phillips et al.*, 2020) with the top layers from ODP U1519. The plate boundary is at a depth of about 7.4 km in the center of our study region, shown by the horizontal dashed line. The sensitivity kernels of 13 s, 14 s, 15 s are plotted in an additional panel to clearly show that the waves with periods shorter than 14 s are sensitive to the upper plate, while the waves with periods longer than 15 s are sensitive to the lower plate. In the frequency domain, we use the data up to 14 s to compute dv/v to focus on the upper plate.

For each station, dv/v from the three cross-components are computed and averaged, using the median and mean values. Component-averaged dv/v on single stations are then averaged from LOBS7,

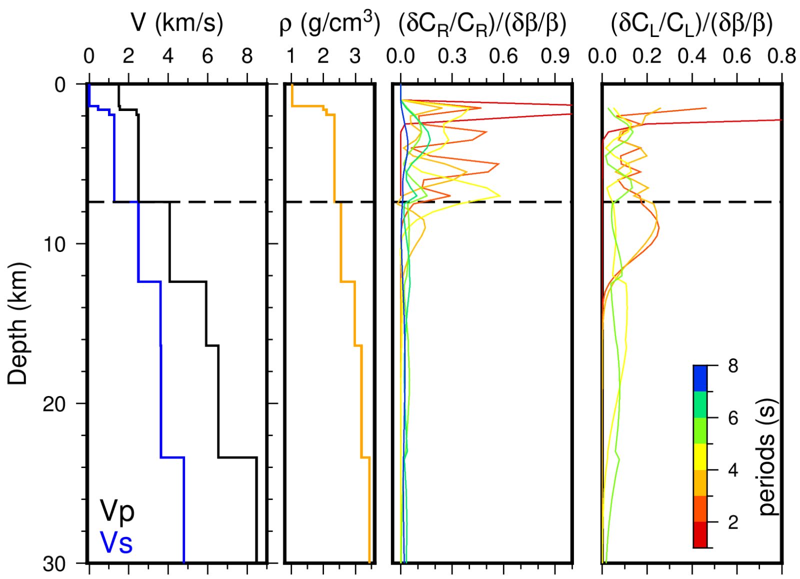

Figure 4. Similar to Figure 3 but for the first overtone mode. Differs from the fundamental mode at 2.5-6 s which is only sensitive to shallow structure (down to 4 km depth), the first overtone mode at 2.5-6 s is also sensitive to shear velocity changes at deeper depth.

LOBS8, LOBS9, and all EOBSs. The errors of the average dv/v are calculated by a bootstrap method. LOBS3 is excluded because it is located on the subducting plate where the SSE2 slip does not reach. The dv/v result from LOBS3 is also less reliable because LOBS3 recorded a dataset with more gaps compared to the other stations (Figure S5).

4 Results

There were four main SSEs (*Warren-Smith et al.*, 2019) during the deployment, for which SSE2 has the most significant displacements, in some locations over 250 mm (Figure 1; *Wallace et al.*, 2016). Many single station results show a velocity decrease during SSE2 and an increase after it (Figure 5). There are also some large changes in velocity outside the time of SSE2 in the single station results. These are mostly suppressed, when we average the single station variations, with the velocity changes around SSE2 and SSE3 left as the most significant in amplitude. We think therefore that stronger variation in individual stations reflects measurement error as a result of low SNR cross-correlation functions. As such, we cannot easily determine a clear spatial variation between results at different stations.

From the average result, there is a 0.06% ± 0.03% velocity decrease during SSE2 over one month and a 0.07% ± 0.04% velocity increase after SSE2 over 1.5 months. This period of velocity decrease extends beyond the period of main slip of SSE2 (red vertical line in Figure 5); however, we cannot easily distinguish when velocities stop decreasing with 20-day stacks. When 10-day stack sizes are used, in comparison, the observed period of velocity decrease instead ends at the time SSE2 finishes its main slip (Figure S10). Following the period of velocity increase after SSE2, the velocity decreases

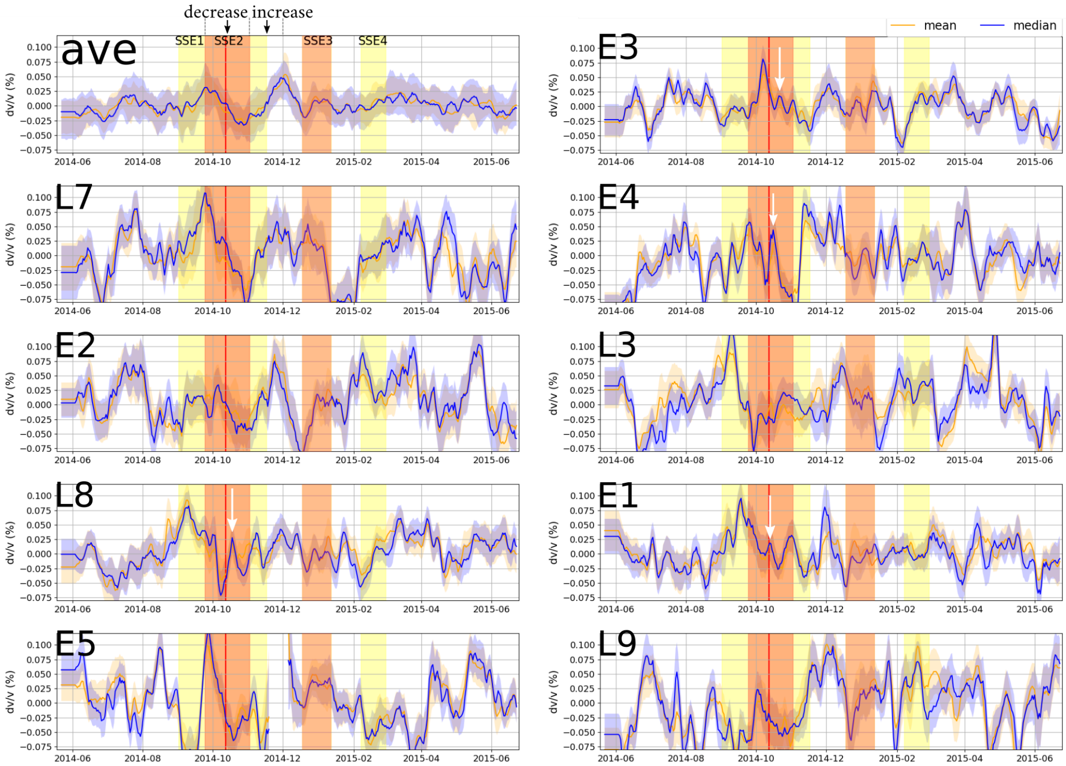

Figure 5. Single station time-dependent velocity variations and their average. Mean (orange) and median (blue) values of velocity variations are shown with their uncertainties for the single-station results and the average result. L3 is not included in the average because it is not in the slip region, and it lost some data (Figure S5). The dv/v values are computed using a 20-day window and further smoothed by a 5-day window. The gap in E5 after SSE2 is because of the lack of data. Four main SSEs during the deployment are marked. SSE2 and SSE3, which had slip under the HOBITSS deployment (Figure S1), are marked by orange. The other two, SSE1 and SSE4, are marked as yellow. The red vertical lines mark the time when SSE2 finishes its main slip. The white arrows indicate some velocity increases after the main slip of SSE2 from some single stations.

$0.06\% \pm 0.03\%$ over 20 days followed by a small increase of $0.03\% \pm 0.03\%$ over 10 days at the reported onset of SSE3, returning to original values.

There are additional periods of large velocity changes outside of the times of slow slip, in particular from July to August 2014. Supporting Information S2 and Figure S12 compare the velocity variations to water pressure, but the water pressure is too small to cause the corresponding velocity changes. These changes are, smaller in magnitude than the changes we observe during and after SSE2. We also note that our velocity changes are relatively small compared to other studies. For example, velocity changes associated with slow slip of about 0.2% were measured by *Rivet et al.* (2011), and 0.5% by *Rivet et al.* (2014), significantly larger than those measured in this study. Fluctuation in velocity change measurements on the order of ±0.02% outside of periods of slow slip is therefore expected. Similarly, the low magnitude of velocity changes means we have relatively large error bars in our average result. However, we demonstrate in the Discussion section that the velocity changes during the period of slow slip, in addition to being the largest recorded, are also well-correlated with measurements from other techniques. Furthermore, we demonstrate that different choices of lag-time window also show the velocity changes as larger around SSE2 and SSE3 than other time periods (Figure S13).

5 Discussion

5.1 Relation to SSEs

The physical mechanism of seismic sources in single station cross component correlations is not yet well understood at large lag-times, and they may contain surface and body waves. This can make a depth analysis of velocity changes complicated, where body waves are expected to have a greater depth sensitivity than surface waves *Obermann et al.* (2013). Determining the relative contribution of surface and body waves is not straightforward. *Obermann et al.* (2013) suggested that surface waves are more dominant at earlier lag times and body waves at later lag times. In contrast, *Yuan et al.* (2021) suggested that, while body waves may contribute equally in the mid-coda, scattered surface waves become dominant again in the late-coda. Acknowledging that this is still an open question, we proceed under the assumption that our measurements are dominated by surface waves following previous studies (e.g., *Hobiger et al.*, 2014). While this is a limitation of our depth analysis, we think it is still useful in discussing the depth that we can expect to sample velocity changes.

Under this assumption, our observations (2.5-14 s) are most sensitive down to 7.4 km depth, based on the sensitivity kernels in figures 3 and 4, which corresponds to the upper plate. Velocity variations with a band pass of 1 to 2.5 s do not show obvious temporal variations (Figure S14), suggesting the changes are not in the very shallow portion of the crust (Figure 3). The temporal velocity variations at 2.5-6 s are similar to those at 2.5-14 s (Figure S10), suggesting that the dominant frequencies of the velocity changes might be 2.5-6 s. The fundamental mode at 2.5-6 s is only sensitive to shallow depths above 4 km (Figure 3), while the first overtone at 2.5-6 s is also sensitive to deeper depths (Figure 4) in the upper plate. The periods 6-14 s also show a velocity decrease during SSE2 and an increase after it (Figure S11), indicating the data still sample the deeper region (4-7.4 km). Our data is limited by poor resolution at depth; the results only reflect an average of the upper plate. Determining the horizontal sensitivity for single-station dv/v measurements is not as straightforward. For a conservative estimate, we consider the maximum distance a surface wave could travel from the network using a velocity of 1.3 km/s (*Yarce et al.*, 2019) and the maximum lag time of our scattered wave window (70s). This equates to a radius of 45 km around the network, approximately the distance from the network to the coast. However, it is unlikely that this radius will be sampled evenly, with dv/v measurements more sensitive to changes within the network (e.g., *De Plaen et al.*, 2019). Because we only observe the changes when all the stations and components are included, we cannot determine a finer-scale variation and it may also indicate that the velocity changes are spread throughout the volume we are sampling.

In summary, the velocity changes we see are likely to be in the top 7 km of the crust, e.g., above the plate interface. Although it is conceptually possible that the changes could be due to a large change in a thin region in the plate interface, we think this is unlikely because the wave periods used are more sensitive to the shallower layers, above about 4 km (Figure 3).

According to the dv/v in the station average (Figure 5 top left), the velocity decrease during SSE2 and increase after SSE2 should be closely related to SSE2. There is a small increase in the station-averaged velocity at the end of October 2014 during SSE2 from the 10-day moving window dv/v (indicated by a white arrow in Figure S10), which is smoothed by the 20-day moving window dv/v results. Some single station 20-day moving window dv/v results (LOBS8, EOBS1, EOBS3, and EOBS4) also show this velocity increase (indicated by white arrows in Figure 5). *Wallace et al.* (2016) suggested the main slip of SSE2 happens before 12th October 2014, while the slip after that until 2nd November 2014 (*Warren-Smith et al.*, 2019) is lower. Thus this velocity increase at the end of October occurred during a tapering-off of slip in SSE2, after the main pulse of slip. Because only some of the stations detect this velocity change, we cannot distinguish whether this is just measurement error, or if it is a real velocity change during the last, lower slip rate phase of SSE2.

Following the velocity increase that ends in early December 2014, the seismic velocity decreases, two weeks prior to the observation of SSE3 on land-based GNSS stations (*Warren-Smith et al.*, 2019). This velocity decrease could be related to SSE3, if SSE3 began in the offshore region earlier than it is seen at the on-land GNSS stations. There are instances at Nankai and Nicoya Peninsula subduction zones of SSE migration (*Araki et al.*, 2017; *Davis et al.*, 2015). Both our velocity decrease and the stress increase (Figure 6; *Warren-Smith et al.*, 2019) started earlier (around 2014-12-02) than the time identified by on-land GNSS stations as the beginning of SSE3 (2014-12-18), suggesting that the SSE may have initiated earlier. However, given that we had limited seafloor geodetic instrument coverage above SSE3 (the main slip of SSE3 is south of the HOBITSS deployment and the slip under the stations is much smaller, < 50 mm, than the SSE2 slip, > 250 mm), it is difficult to determine SSE3 timing offshore. In contrast, SSE2 timing is determined using on-land GNSS data, and offshore APG data have an offset during SSE2, confirming the general timing of the SSE2 peak slip (*Wallace et al.*, 2016). The SSE3 timing suggested by the velocity decrease is from the beginning of December, lasting approximately 20 days. After that, velocity recovery occurs over approximately 10 days, possibly reflecting fluid diffusion and/or changes in porosity.

SSE1 and SSE4 are smaller and do not occur under the deployment region (*Warren-Smith et al.*, 2019) and therefore are not expected to influence velocity changes.

We suggest two hypotheses based on our observations, both of which assume that the velocity changes take place in a broad region within the upper plate. 1) Fluid migration related to fault-valve behavior: the velocity decrease during SSE2 is caused by fluids migrating into the upper plate as SSE2 breaks a low-permeability seal on the plate boundary. 2) Crustal strain changes through the SSE cycle: the velocity decrease during SSE2 is caused by increased porosity because SSE2 relieves the elastic strain, which results in dilation. A combination of both processes is also possible.

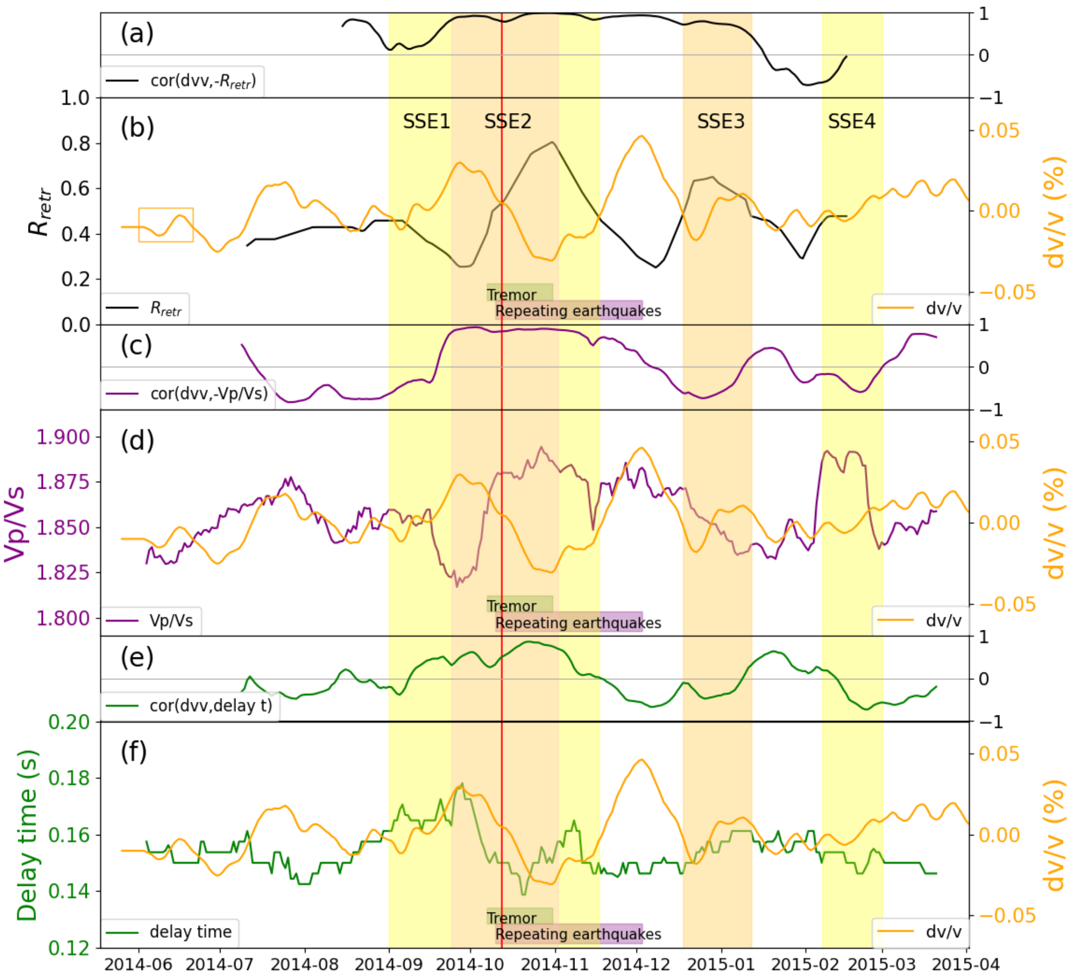

327 **Figure 6.** The median value of 20-day moving window station-average velocity variations compared to other studies. Four
328 SSEs are marked and the vertical red line marks the time when SSE2 finishes its main slip (*Wallace et al.*, 2016; *Warren-*
329 *Smith et al.*, 2019). (b), (d), (f) are to compare with other studies and (a), (c), (e) are the corresponding correlations. (a) corre-
330 lation of velocity variations and inverted stress ratio variations (by inverted we mean that the stress ratio curve is multiplied by
331 -1), computed using a 35-day moving window and a step of 1 day. The grey horizontal line marks value 0 of correlation. The
332 top and bottom are 1 and -1 respectively. (b) velocity variations compared to retrieved stress ratio variations Rretr. The black
333 curve shows stress ratio changes (*Warren-Smith et al.*, 2019), which focus on the lower plate. The orange curve shows the
334 velocity variations, which focus on the upper plate. The yellow rectangle shows a 20-day window length. The time duration
335 of tremor (*Todd et al.*, 2018) and repeating earthquakes (*Shaddox and Schwartz*, 2019) are denoted by green shade and purple
336 shade respectively. (c) correlation of velocity variations and inverted Vp/Vs variations [from *Zal et al.* (2020)]. (d) velocity
337 variations compared with Vp/Vs variations. (e) correlation of velocity variations and delay time variations [from *Zal et al.*
338 (2020)]. (f) velocity variations compared with delay time variations.

5.2 Fluid migration related to fault-valve behavior

Seismic velocity changes, especially for shear waves, have often been related to fluid changes. Fluids exist in several forms and influence seismic velocities in different ways (*Berryman*, 2007). Free water can be present in near surface water tables in very shallow regions (hundreds of meters) and bound water appears in minerals (mainly in the mantle and lower crust). In our case, the velocity variations are likely to be linked with free water. Fluid volume increase in pores or cracks leads to a shear velocity decrease (*Grêt et al.*, 2006). Surface waves are sensitive to fluid volume, with an increase in fluid volume corresponding to a shear velocity decrease, and vice versa (*Grêt et al.*, 2006). The velocity decrease observed is therefore consistent with a fluid volume increase in the upper plate during SSE2. After SSE2, the velocity increase suggests the fluids in the upper plate diffuse over time.

Warren-Smith et al. (2019) and *Zal et al.* (2020) both support a 'fault-valve' hypothesis in this region of the Hikurangi margin, wherein a temporary low-permeability seal on the plate boundary maintains near lithostatic fluid pressure in the lower plate, which accumulates over time, reaching a peak prior to slow slip, which might trigger slip initiation. Following this, the occurrence of slow slip ruptures the seal and fluids migrate from the interface to the upper plate.

Here we compare the velocity variations in the upper plate with the stress ratio variations in the lower plate (Figure 6b; *Warren-Smith et al.*, 2019), Vp/Vs and delay time variations in the upper plate (Figure 6d and f; *Zal et al.*, 2020). The temporal stress ratio variations and velocity variations might have a time shift (Figure 6) because the stress ratio variations have horizontal uncertainties varying from ±2 to ±13 days (*Warren-Smith et al.*, 2019). *Zal et al.* (2020) used a 20-day centered moving window for Vp/Vs and delay time computations, whereas our velocity variations are smoothed and represent the average of that particular day and the 19 previous. To better compare the results, we shift the variations of *Zal et al.* (2020) to the right by 10 days. The dv/v variations around SSE2 are negatively correlated with the stress ratio (Figure 6b) and the Vp/Vs variations (Figure 6d), and are in good positive correlation with delay time variations (Figure 6f). The stress ratio increases while the velocity decreases during SSE2. Since the stress ratio has a negative correlation with pore fluid pressure, this suggests a fluid pressure decrease in the top of the subducting plate during SSE2 (as the impermeable seal at the plate interface is broken during the SSE). Likewise, the velocity decrease that we observe along with the Vp/Vs ratio increase as well as the delay time decrease observed by *Zal et al.* (2020) suggest an increase in the amount of interconnected fluids in the upper plate during SSE2. After SSE2, the plate boundary reseals, and the fluid pressure gradually builds up again beneath the low-permeability boundary (producing a decrease in the stress ratio; Warren-Smith et al., 2019; Figure 6b) The fluids in the upper plate dissipate over time, producing an increase in velocity and a decrease in Vp/Vs (Zal et al., 2020; Figure 6d). Together, these observations support the suggestion of *Warren-Smith et al.* (2019) that fault valve behaviour may regulate the timing and occurrence of SSEs (Figure 7a). Although the lower plate region sampled by stress ratio changes (*Warren-Smith et al.*, 2019) is not within the footprint of the HOBITSS network (but closer to the coast), there may be some fluids coming from the interface, or from the slab underneath the network, which have not been resolved with the focal mechanism catalogues (*Warren-Smith et al.*, 2019). Although the volume and pathway of the fluids is largely unconstrained, our observation of decreased velocity is consistent with fluid migration into the upper plate during SSE2 (*Zal et al.*, 2020).

Periods of both burst-type repeating earthquakes (*Shaddox and Schwartz*, 2019) and tremor (*Todd et al.*, 2018) were observed during and after SSE2 (shown in Figure 6). The repeating earthquakes are suggested to occur on an upper-plate fracture network above the subducted seamount, lasting about two months. The timing of repeating earthquake activity spans both a period of velocity decrease during SSE2, and the subsequent velocity increase. A possible explanation can be found in the relative timing and location of the repeating earthquake activity. The majority of the repeating earthquakes occurred following the end of the SSE2 main slip, with *Shaddox and Schwartz* (2019) arguing that these, along with the tectonic tremor, were triggered by the migration of fluid from over-pressured sediments down-dip of the seamount into the upper plate fracture network. The time needed for fluids to migrate from the interface to the surface is on the order of days to weeks. We suggest that the velocity decrease we observe during SSE2 could be associated with the initial migration of fluids from the interface into the upper plate, which triggered the repeating earthquakes during SSE2. The subsequent velocity increase may be associated with diffusion of fluids through the upper plate after SSE2, which could also be responsible for triggering the repeating earthquakes. The geophysical signatures of fluid movement depend on the pathways that the fluids take and the amount of fluids migrating. Drawing direct correlations between variations in crustal velocities, repeating earthquakes, and fluid migration events remains challenging. Upper plate fluid migration models are required to test the timing difference.

The patterns of temporal variations of the velocity and the stress ratio for SSE3 are also broadly consistent (if the velocity variations are caused by SSE3). Before SSE3, the decrease in stress ratio implies a fluid pressure accumulation in the lower plate related to the presence of a low-permeability seal, while an increase in velocity is caused by fluids diffusing out of the upper plate following SSE2 (Figure 7a). Subsequently, the increase in stress ratio and the decrease in velocity start a week or two earlier than the timing of SSE3 observed from onshore GNSS stations. However, it is plausible that SSE3 began earlier in the offshore region, out of reach of the onshore GNSS stations; this supposition is consistent with the stress ratio (*Warren-Smith et al.*, 2019) and seismic velocity changes.

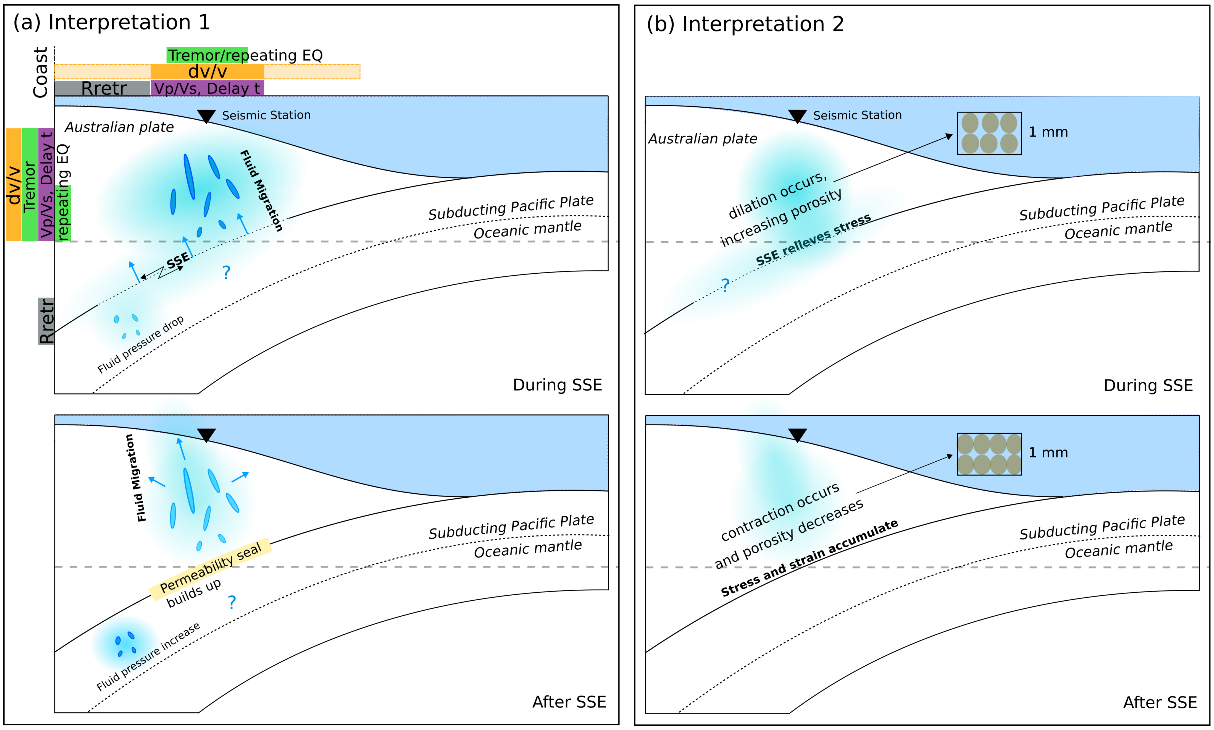

Figure 7. Model adapted after *Husen and Kissling* (2001) and *Zal et al.* (2020). The horizontal grey dashed lines mark the depth of our observation under the seismic station, referring to the sensitivity kernels (Figure 3). The bars on the top of Figure (a) show the horizontal space coverage of different data (Figure 6), and the bars on the left of Figure (a) show the corresponding vertical space coverage. The main observation of dv/v is considered to be under the network (orange), though it is possible that it extends over a wider region (light orange). Here we give two interpretations. A combination of both processes is also possible. (a) Interpretation 1: Fluid migration. During the SSE, the low-permeability seal on the plate boundary is broken. This allows the interconnected fluids around the interface to migrate to the upper plate, causing a seismic velocity decrease in the upper plate. In the lower plate, *Warren-Smith et al.* (2019) observed a fluid pressure drop near the coast. However, we do not have constraints for the lower plate within the footprint of the HOBITSS network. After the SSE, the fluids in the upper plate diffuse and the seismic velocity increases. The permeability seal on the plate interface establishes itself, and the fluid pressure in the lower plate starts to re-accumulate. The color bars on the top left give the spatial correlation of observations obtained using different geophysical methodologies. Horizontally, velocity variations (orange) mainly sample under the HOBITSS deployment (Figure 1) with an extension (light orange) estimated according to the scattered wave window length and Vs (*Yarce et al.*, 2019). Vertically, velocity variations sample the upper plate according to the sensitivity kernel (Figure 3). Rretr variations (grey) sample the lower plate between the HOBITSS deployment and the coast where most of the earthquakes used in *Warren-Smith et al.* (2019) are located. The variations of Vp/Vs and delay time (purple) sample the upper plate under the HOBITSS deployment according to the paths of the earthquakes used in *Zal et al.* (2020). The region where the tremor and repeating earthquakes (green) occurred are extracted from *Todd et al.* (2018) and *Shaddox and Schwartz* (2019). They occur in the same horizontal location, but vertically repeating earthquakes are only in the bottom half of the region where the tremor may be active. (b) Interpretation 2: crustal strain changes through the SSE cycle. During the SSE, the occurrence of SSE relieves stress, resulting in dilation and an increase of porosity, which in turn decreases the velocity. With the increase of porosity, there might be an increase in fluid volume. After the SSE, the subduction interface re-locks and contractional elastic strain starts to accumulate and squeeze the materials, resulting in a decrease of porosity and increase in velocity between SSEs.

5.3 Assessing our observations in terms of porosity changes due to crustal strain

We test our assumption that the velocity changes are due to pervasive voids in the upper plate by an order-of-magnitude estimate of the porosity changes that would be required to create the observed velocity changes. Because the velocity changes are difficult to measure, it is impossible to determine their exact location. In addition, our understanding of the exact stratigraphy in the region is limited, and the relation between velocity and porosity is poorly constrained, so the calculation is inexact. In particular, if the velocity changes occur in only a small part of the crust, the porosity changes may be underestimated.

The outer forearc overlying the shallow SSE region of north Hikurangi is thought to be largely composed of Miocene to recent sediments of the East Coast Basin (analogous to the Tolaga Group exposed in the adjacent onshore region (*Mazengarb and Speden*, 2000)), consisting of interlayered mudstones, sandstones, and occasional limestones (*Neef and Bottrill*, 1992; *Wallace et al.*, 2019). According to previous studies (*Gardner et al.*, 1974; *Eberhart-Phillips et al.*, 1989; *Bassett et al.*, 2014), the porosity in our study region is about 20% to 35%. Assuming a Vs of 1.3 km/s (*Yarce et al.*, 2019), and based on the relationship of Vs and porosity ϕ (*Mavko et al.*, 2020; *Hoffman and Tobin*, 2002), the velocity decreases 0.06% during SSE2 and so the effective porosity increases on the order of 0.0001%, and the percentage change of porosity is about from $0.0001\%/35\% \times 100\% = 0.0003\%$ to $0.0001\%/20\% \times 100\% = 0.0005\%$. The velocity decrease can be explained by small changes in porosity resulting from crustal strain acting on the upper plate during the SSE, which places the upper plate overlying the SSE source into dilation. The occurrence of SSE2 relieves the accumulated stress and strain recovers elastically, which results in dilation. The porosity then increases, and velocity decreases. After SSE2, the fault resumes inter-SSE locking, and the upper plate experiences contraction as elastic strain accumulates, causing the porosity to steadily decrease and velocity to increase (Figure 7b).

Whereas we estimate the change in porosity using changes in shear-wave velocity, the elastic moduli of accretionary prism rocks can be used independently to estimate the positive volume change (dilation) expected to result from the reduction in stress coincident with an SSE. Assuming an average prism sediment Vs = 1300 m/s (*Yarce et al.*, 2019), a sediment density of $\rho = 2300 kg/m^3$ (*Eberhart-Phillips et al.*, 2020), the shear modulus, G, is equal to approximately 4 GPa (where $Vs = \sqrt{G/\rho}$). Using an average prism sediment Vp = 2300 m/s (*Yarce et al.*, 2019), the bulk modulus K is approximately 7 GPa (where $Vp = \sqrt{(K + 4G/3)/\rho}$). From the bulk modulus, we can then calculate the volume change expected for the prism sediments following slip during the SSE, which results in a stress drop given by $\delta\sigma_{static} = Gd/w$ (*Stein and Wysession*, 2009). Where G is the shear modulus, d is the amount of slip, and w is the down-dip width of the fault. For the displacement (d= 0.27 m) and down-dip width of the fault (w = 33000 m) measured in SSE2 (*Wallace et al.*, 2016), $\delta\sigma_{static}$ is estimated to be 30 kPa. A 30 kPa stress drop equates with a percent volume change of 0.0004% using the relationship $K = \delta\sigma_{static}/(\delta V/V)$. This volume change, derived from the estimated stress drop and measured bulk modulus of the hanging wall sediments, concurs with the percent change in porosity (0.0003% to 0.0005%) estimated from seismic velocity variations. We propose that given sufficient resolution, seismic velocity variations may be capable of monitoring minute strains in the hanging wall of subduction zone megathrusts.

Rivet et al. (2011) studied velocity variations at 7-17 s, corresponding to the depth of 5-20 km (upper and middle crust), related to the 2006 Mexico SSE. Following this, *Rivet et al.* (2014) observed velocity variations at 12-24 s, corresponding to the depth of 10-30 km (middle and lower crust), related to the 2009-2010 Mexico SSE. They discussed that there are possible velocity variations at longer periods and deeper depths (*Rivet et al.*, 2014). Table S2 compares the velocity variations associated with the 2006 and 2009-2010 Mexico SSEs (*Rivet et al.*, 2011, 2014) with this study.

Rivet et al. (2011) computed the static strain field associated with the 2006 Mexico SSE, which showed that the SSE produced an extended increase in dilation. This coincides with our interpretation of crustal strain changes through the SSE cycle. However, volumetric deformation ($\sim 10^{-6}$) estimated during the 2006 Mexico SSE was much smaller than the volume change that they estimated ($\sim 10^{-3}$) from their velocity change, suggesting that the velocity change was related to the strain rate rather than the strain itself (*Rivet et al.*, 2011). The finding from *Rivet et al.* (2014) for the 2009-2010 Mexico SSE supported this conclusion. During the 2014 Gisborne SSE2 in this study, however, our estimated percent volume change (0.0004%), derived from the estimated stress drop and bulk modulus of the hanging wall sediments, concurs with the percent porosity change (0.0003% to 0.0005%) estimated from seismic velocity variations. Therefore, if the observed velocity change is due to a change in porosity, we suggest it is related to strain. *Rivet et al.* (2014) found significant correlation between tremor and velocity variations during the SSE, suggesting that these two independent observations can be linked to the same mechanism. For the 2014 Gisborne SSE2, however, both the tremor and repeating earthquakes occurred slightly later than the start of SSE2 and the measured velocity decrease. This is particularly obvious for the repeating earthquakes, which occurred until the velocity increased to its peak. The velocity variations may be either partly or fully controlled by the strain/volume changes. Fluid migration, which can trigger the tremor and repeating earthquakes, may happen later or over a longer time period.

6 Conclusions

We analyse one-year ambient noise data acquired by nine OBSs deployed in the northern Hikurangi Margin in a region where SSEs occur. During the deployment (May 2014 - June 2015), there were four SSEs (*Warren-Smith et al.*, 2019), with the strongest of them (SSE2) occurring from September to October 2014, lasting five weeks. We compute temporal velocity variations using scattered waves retrieved from single station cross component correlations. The average velocity variations exhibit a velocity decrease during SSE2 and a velocity increase after SSE2. The velocity variations fit well with the variations of stress ratio, Vp/Vs, and shear-wave splitting delay times from other studies (*Warren-Smith* *et al.*, 2019; *Zal et al.*, 2020; *Shaddox and Schwartz*, 2019; *Todd et al.*, 2018). After SSE2, the velocity decrease followed by an increase returning to original values might be caused by SSE3.

We give two possible end-member interpretations: 1) Fluid migration related to fault-valve behavior between the two plates: Before SSE2, there is a permeability seal on the plate boundary that traps fluid beneath the subduction interface and fluid pressure steadily increases, to the point at which the SSE is triggered (*Warren-Smith et al.*, 2019). The occurrence of SSE2 breaks the seal on the plate boundary and trapped fluids migrate to the upper plate. The fluid migration takes place over approximately one month from late September to the start of November 2014. We observe a velocity decrease in the upper plate consistent with increased fluid volume in the upper plate. After SSE2, the plate boundary re-seals and the fluids in the upper plate diffuse, and velocity begins increasing again. This happens after SSE2 until around 1st December 2014. This interpretation is consistent with that of *Warren-Smith et al.* (2019) and *Zal et al.* (2020). 2) Crustal strain changes through the SSE cycle: Before SSE2, the plates are locked together along the plate interface, and elastic strain (largely contraction) accrues in the overriding plate. The occurrence of SSE2 relieves the accumulated elastic strain, resulting in dilation and an increase of porosity. This takes place over approximately one month from late-September to the start of November 2014. We observe a velocity decrease in the upper plate, which may be consistent with increased porosity. A porosity increase can lead to an increase of fluid volume. After SSE2, the plate boundary re-locks and contraction begins again, resulting in a subsequent porosity decrease and velocity increase. This happens after SSE2 until around 1st December 2014.

We point out that aspects of both the interpretations may be at play to explain the observed seismic velocity changes. Both of them can possibly lead to fluid volume changes, but the volume and pathway of the fluids are unconstrained. A combination of fluid migration related to fault-valve behavior and consequences of crustal strain during the SSE may explain both this study and previous research (*Warren-Smith et al.*, 2019; *Zal et al.*, 2020; *Shaddox and Schwartz*, 2019; *Todd et al.*, 2018). Our study shows that velocity variations associated with the occurrence of SSEs in New Zealand are detectable using ambient noise interferometry, and results provide new evidence to support the integral role fluids and accumulated elastic strain energy play in promoting SSEs on the northern Hikurangi Margin.

Acknowledgments

This research was supported by an Endeavour Fund grant (funding contract C05X1605) from Ministry of Business, Innovation and Employment. The ocean bottom seismic data were provided by instruments from the Ocean Bottom Seismograph Instrument Pool (https://www.iris .edu /hq /programs /obsip), funded by the National Science Foundation (NSF): OCE-1333311, OCE-1551683, OCE-1333025, OCE-1334654, OCE-1551922; and the Earthquake Research Institute (ERI), University of Tokyo, funded by JSPS KAKENHI: JP16H06475. Additional funding support came from strategic science investment funding (SSIF) to GNS Science from MBIE (C05X1909 Resilience to Nature's Challenges Kia Manawaroa - Nga Akina o Te Ao Turoa) and the National Science Challenges (RNC2). Raw data from the experiment is archived at Incorporate Research Institutions for Seismology Data Management Center (IRIS-DMC) with experiment codes YH 2014-15 (seismic data) and 8F 2014-15 (bottom pressure record data).

We acknowledge the HOBITSS project, and Tangaroa cruise TAN1405 to collect the data. We acknowledge MSNoise 1.5, which supports this study technically. We also acknowledge Pasan Herath, Katherine Woods, Katrina Jacobs, Susan Schwartz, and Heather Shaddox for their helpful feedback and discussion.

References

Araki, E., D. M. Saffer, A. J. Kopf, L. M. Wallace, T. Kimura, Y. Machida, S. Ide, E. Davis, I. Expedition, et al. (2017), Recurring and triggered slow-slip events near the trench at the Nankai Trough subduction megathrust, *Science*, *356*(6343), 1157–1160.

Bassett, D., R. Sutherland, and S. Henrys (2014), Slow wavespeeds and fluid overpressure in a region of shallow geodetic locking and slow slip, Hikurangi subduction margin, New Zealand, *Earth and Planetary Science Letters*, *389*, 1–13.

Berryman, J. G. (2007), Seismic waves in rocks with fluids and fractures, *Geophysical Journal International*, *171*(2), 954–974.

Brenguier, F., M. Campillo, C. Hadziioannou, N. M. Shapiro, R. M. Nadeau, and E. Larose (2008), Postseismic Relaxation Along the San Andreas Fault at Parkfield from Continuous Seismological Observations, *Science*, *321*(5895), 1478–1481, doi:10.1126/science.1160943.

Chaves, E. J., and S. Y. Schwartz (2016), Monitoring transient changes within overpressured regions of subduction zones using ambient seismic noise, *Science Advances*, *2*(1), doi:10.1126/sciadv.1501289.

Clarke, D., L. Zaccarelli, N. M. Shapiro, and F. Brenguier (2011), Assessment of resolution and accuracy of the Moving Window Cross Spectral technique for monitoring crustal temporal variations using ambient seismic noise, *Geophysical Journal International*, *186*(2), 867–882, doi:10.1111/j.1365-246X.2011.05074.x.

Coffin, M., L. Gahagan, and L. Lawver (1998), Present-day plate boundary digital data compilation, *University of Texas Institute for geophysics technical report*, *174*(5).

Davis, E. E., H. Villinger, and T. Sun (2015), Slow and delayed deformation and uplift of the outermost subduction prism following ETS and seismogenic slip events beneath Nicoya Peninsula, Costa Rica, *Earth and Planetary Science Letters*, *410*, 117–127.

De Plaen, R. S., A. Cannata, F. Cannavo, C. Caudron, T. Lecocq, and O. Francis (2019), Temporal changes of seismic velocity caused by volcanic activity at Mt. Etna revealed by the autocorrelation of ambient seismic noise, *Frontiers in Earth Science*, *6*, 251.

Eberhart-Phillips, D., D.-H. Han, and M. Zoback (1989), Empirical relationships among seismic velocity, effective pressure, porosity, and clay content in sandstone, *Geophysics*, *54*(1), 82–89.

Eberhart-Phillips, D., S. Bannister, M. Reyners, and S. Henrys (2020), New Zealand Wide model 2.2 seismic velocity and Qs and Qp models for New Zealand, doi:10.5281/zenodo.3779523.

Frank, W. B., N. M. Shapiro, A. L. Husker, V. Kostoglodov, H. S. Bhat, and M. Campillo (2015), Along-fault pore-pressure evolution during a slow-slip event in Guerrero, Mexico, *Earth and Planetary Science Letters*, *413*, 135–143.

Gardner, G., L. Gardner, and A. Gregory (1974), Formation velocity and density—The diagnostic basics for stratigraphic traps, *Geophysics*, *39*(6), 770–780.

Gosselin, J. M., P. Audet, C. Estève, M. McLellan, S. G. Mosher, and A. J. Schaeffer (2020), Seismic evidence for megathrust fault-valve behavior during episodic tremor and slip, *Science advances*, *6*(4), eaay5174.

Grêt, A., R. Snieder, and J. Scales (2006), Time-lapse monitoring of rock properties with coda wave interferometry, *Journal of Geophysical Research: Solid Earth*, *111*(B3), doi:10.1029/2004JB003354.

Harmon, N., D. Forsyth, and S. Webb (2007), Using ambient seismic noise to determine short-period phase velocities and shallow shear velocities in young oceanic lithosphere, *Bulletin of the Seismological Society of America*, *97*(6), 2009–2023.

Hobiger, M., U. Wegler, K. Shiomi, and H. Nakahara (2014), Single-station cross-correlation analysis of ambient seismic noise: application to stations in the surroundings of the 2008 Iwate-Miyagi Nairiku earthquake , *Geophysical Journal International*, *198*(1), 90–109, doi:10.1093/gji/ggu115.

Hoffman, N. W., and H. J. Tobin (2002), An empirical relationship between velocity and porosity for underthrust sediments of the Nankai Trough Accretionary Prism, in *AGU Fall Meeting Abstracts*, vol. 2002, pp. T62C–1328.

Husen, S., and E. Kissling (2001), Postseismic fluid flow after the large subduction earthquake of Antofagasta, Chile, *Geology*, *29*(9), 847–850.

Ito, Y., R. Hino, M. Kido, H. Fujimoto, Y. Osada, D. Inazu, Y. Ohta, T. Iinuma, M. Ohzono, S. Miura, et al. (2013), Episodic slow slip events in the Japan subduction zone before the 2011 Tohoku-Oki earthquake, *Tectonophysics*, *600*, 14–26.

Larose, E., P. Roux, and M. a. Campillo (2007), Reconstruction of Rayleigh–Lamb dispersion spectrum based on noise obtained from an air-jet forcing, *The Journal of the Acoustical Society of America*, *122*(6), 3437–3444, doi:10.1121/1.2799913.

Lecocq, T., C. Caudron, and F. Brenguier (2014), MSNoise, a Python Package for Monitoring Seismic Velocity Changes Using Ambient Seismic Noise, *Seismological Research Letters*, *85*(3), 715–726, doi:10.1785/0220130073.

Martínez-Garzón, P., V. Vavryčuk, G. Kwiatek, and M. Bohnhoff (2016), Sensitivity of stress inversion of focal mechanisms to pore pressure changes, *Geophysical Research Letters*, *43*(16), 8441–8450.

Mavko, G., T. Mukerji, and J. Dvorkin (2020), *The rock physics handbook*, Cambridge university press.

Mazengarb, C., and I. Speden (2000), Geology of the Raukumara area, Geol.

Nakajima, J., and N. Uchida (2018), Repeated drainage from megathrusts during episodic slow slip, *Nature Geoscience*, *11*(5), 351–356.

Neef, G., and R. Bottrill (1992), The Cenozoic geology of the Gisborne area (1: 50 000 metric sheet Y18AB), North Island, New Zealand, *New Zealand journal of geology and geophysics*, *35*(4), 515–531.

Obermann, A., T. Planes, E. Larose, C. Sens-Schönfelder, and M. Campillo (2013), Depth sensitivity of seismic coda waves to velocity perturbations in an elastic heterogeneous medium, *Geophysical Journal International*, *194*(1), 372–382.

Poupinet, G., W. L. Ellsworth, and J. Frechet (1984), Monitoring velocity variations in the crust using earthquake doublets: An application to the Calaveras Fault, California, *Journal of Geophysical Research: Solid Earth*, *89*(B7), 5719–5731, doi:10.1029/JB089iB07p05719.

Rivet, D., M. Campillo, N. M. Shapiro, V. Cruz-Atienza, M. Radiguet, N. Cotte, and V. Kostoglodov (2011), Seismic evidence of nonlinear crustal deformation during a large slow slip event in Mexico, *Geophysical Research Letters*, *38*(8), doi:10.1029/2011GL047151.

Rivet, D., M. Campillo, M. Radiguet, D. Zigone, V. Cruz-Atienza, N. M. Shapiro, V. Kostoglodov, N. Cotte, G. Cougoulat, A. Walpersdorf, et al. (2014), Seismic velocity changes, strain rate and non-volcanic tremors during the 2009–2010 slow slip event in Guerrero, Mexico, *Geophysical Journal International*, *196*(1), 447–460.

Russell, J. B., J. B. Gaherty, P.-Y. P. Lin, D. Lizarralde, J. A. Collins, G. Hirth, and R. L. Evans (2019), High-resolution constraints on Pacific upper mantle petrofabric inferred from surface-wave anisotropy, *Journal of Geophysical Research: Solid Earth*, *124*(1), 631–657.

Saffer, D. M., and H. J. Tobin (2011), Hydrogeology and Mechanics of Subduction Zone Forearcs: Fluid Flow and Pore Pressure, *Annual Review of Earth and Planetary Sciences*, *39*(1), 157–186, doi: 10.1146/annurev-earth-040610-133408.

Schwartz, S. Y., and J. M. Rokosky (2007), Slow slip events and seismic tremor at circum-Pacific subduction zones, *Reviews of Geophysics*, *45*(3).

Shaddox, H. R., and S. Y. Schwartz (2019), Subducted seamount diverts shallow slow slip to the forearc of the northern Hikurangi subduction zone, New Zealand, *Geology*, *47*(5), 415–418, doi: 10.1130/G45810.1.

Stein, S., and M. Wysession (2009), *An introduction to seismology, earthquakes, and earth structure*, John Wiley & Sons.

TAN1405 Science Party, E. c., Todd (2014), TAN1405 Voyage Report: Hikurangi Ocean Bottom Investigation of Tremor and Slow Slip (HOBITSS), *RV Tangaroa*, *10-20 May 2014*, Lower Hutt, N.Z.: GNS Science. GNS Science report 2014/67 86 p. + 1 CD–Rom.

Todd, E. K., S. Y. Schwartz, K. Mochizuki, L. M. Wallace, A. F. Sheehan, S. C. Webb, C. A. Williams, J. Nakai, J. Yarce, B. Fry, S. Henrys, and Y. Ito (2018), Earthquakes and Tremor Linked to Seamount Subduction During Shallow Slow Slip at the Hikurangi Margin, New Zealand, *Journal of Geophysical Research: Solid Earth*, *123*(8), 6769–6783, doi:10.1029/2018JB016136.

Wallace, L., D. Saffer, P. Barnes, I. Pecher, K. Petronotis, and L. LeVay (2019), Site U1519.

Wallace, L. M., and J. Beavan (2010), Diverse slow slip behavior at the Hikurangi subduction margin, New Zealand, *Journal of Geophysical Research: Solid Earth*, *115*(B12), doi:10.1029/2010JB007717.

Wallace, L. M., S. C. Webb, Y. Ito, K. Mochizuki, R. Hino, S. Henrys, S. Y. Schwartz, and A. F. Sheehan (2016), Slow slip near the trench at the Hikurangi subduction zone, New Zealand, *Science*, *352*(6286), 701–704, doi:10.1126/science.aaf2349.

Warren-Smith, E., B. Fry, L. Wallace, E. Chon, S. A. Henrys, A. F. Sheehan, K. Mochizuki, S. Y. Schwartz, and S. Lebedev (2019), Episodic stress and fluid pressure cycling in subducting oceanic crust during slow slip, *Journal of Geophysical Research: Solid Earth*, doi:10.1038/s41561-019-0367-x.

Wessel, P., W. H. Smith, R. Scharroo, J. Luis, and F. Wobbe (2013), Generic mapping tools: improved version released, *Eos, Transactions American Geophysical Union*, *94*(45), 409–410.

Williams, C. A., D. Eberhart-Phillips, S. Bannister, D. H. N. Barker, S. Henrys, M. Reyners, and R. Sutherland (2013), Revised Interface Geometry for the Hikurangi Subduction Zone, New Zealand, *Seismological Research Letters*, *84*(6), 1066–1073, doi:10.1785/0220130035.

Yarce, J., A. F. Sheehan, J. S. Nakai, S. Y. Schwartz, K. Mochizuki, M. K. Savage, L. M. Wallace, S. A. Henrys, S. C. Webb, Y. Ito, R. E. Abercrombie, B. Fry, H. Shaddox, and E. K. Todd (2019), Seismicity at the Northern Hikurangi Margin, New Zealand, and Investigation of the Potential Spatial and Temporal Relationships With a Shallow Slow Slip Event, *Journal of Geophysical Research: Solid Earth*, *124*(5), 4751–4766, doi:10.1029/2018JB017211.

Yates, A. (2018), Seismic velocity changes at White Island volcano, New Zealand, using ten years of ambient noise interferometry.

Yates, A. S., M. K. Savage, A. D. Jolly, C. Caudron, and I. J. Hamling (2019), Volcanic, Coseismic, and Seasonal Changes Detected at White Island (Whakaari) Volcano, New Zealand, Using Seismic Ambient Noise, *Geophysical Research Letters*, *46*(1), 99–108, doi:10.1029/2018GL080580.

Yuan, C., J. Bryan, and M. Denolle (2021), Numerical comparison of time-, frequency-and wavelet-domain methods for coda wave interferometry, *Geophysical Journal International*, *226*(2), 828–846.

Zal, H. J., K. Jacobs, M. K. Savage, J. Yarce, S. Mroczek, K. Graham, E. K. Todd, J. Nakai, Y. Iwasaki, A. Sheehan, K. Mochizuki, L. Wallace, S. Schwartz, S. Webb, and S. Henrys (2020), Temporal and spatial variations in seismic anisotropy and VP/VS ratios in a region of slow slip, *Earth and Planetary Science Letters*, *532*, 115,970, doi:https://doi.org/10.1016/j.epsl.2019.115970.

Published in *EPSL; DOI: 10.1016/j.epsl.2022.117443*

Supporting Information for Velocity variations in the northern Hikurangi margin and the relation to slow slip

Weiwei Wang[1,2], Martha K. Savage[1], Alexander Yates[1,3], Hubert J. Zal[1], Spahr Webb[4], Carolyn Boulton[1], Emily Warren-Smith[5], Megan Madley[1,5], Tim Stern[1], Bill Fry[5], Kimihiro Mochizuki[6], Laura Wallace[5,7]

[1]Victoria University of Wellington, Wellington, New Zealand
[2]The University of Auckland, Auckland, New Zealand
[3]Université Grenoble Alpes, Université Savoie Mont Blanc, CNRS, IRD, IFSTTAR, ISTerre, 38000 Grenoble, France
[4]Lamont-Doherty Earth Observatory, Columbia University, Palisades, NY, USA
[5]GNS Science, Lower Hutt, New Zealand
[6]Earthquake Research Institute, University of Tokyo, Tokyo, Japan
[7]University of Texas Institute for Geophysics, Austin, TX, USA

Contents of this file

Introduction

The supporting information contains additional details about data processing and analysis to support the Method and Discussion sections in the main text.

Text S1. Parameterization

Parameters in MSNoise are tested before they are determined. Different filter ranges are tested and compared with lag-time dependent SNR: The signal is the Hilbert envelope of an average of single-day cross-correlations, while the noise is computed by measuring the variation of single-day cross-correlations at each lag time (*Larose et al.*, 2007; *Clarke et al.*, 2011). Figure S2 shows an example on LOBS8 vertical-parallel component correlations, shown with its waveform for a better understanding of the lag-time dependent SNR. Other components of LOBS8 and other stations have the same features: the filters of 2.5-6 s and 2.5-20 s have high SNR for the scattered waves. Segmentation length (raw data window length to correlate), segmentation overlap (overlap in window length between segments), normalization (1-bit, or windsorizing at N time Root-Mean-Square), are determined by lag-time dependent SNR. Figure S3 shows examples for how segmentation length and overlap are determined. The ones leading to the highest SNR are used.

Current stack size is determined by correlation coefficients between current stacks and the reference stack. A large size of the current stack can decrease the temporal resolution and might hide some velocity changes happening in a short time, but too small size of the stack might not be enough to suppress noise. Correlation coefficients between different size current stacks and the reference stack are computed and compared (Figure S4) using the full stacks (-300 s to 300 s lag time). Before stacking for both current stacks and the reference stack, the single day stacks with correlation coefficients smaller than a threshold (Figure S4 caption) are taken out to exclude noisy data. The threshold varies from station to station.

The scattered wave window on the cross-correlations to compute velocity variations is determined by lag-time dependent SNR (Figure S8), with the SNR of all the single stations larger than 2. The SNR threshold follows previous studies *Yates* (2018); *Yates et al.* (2019). MSNoise selects data by the coherence. The coherence threshold is determined by the relationship between SNR and coherence to exclude the data with SNR < 2. The scattered wave window on the negative lag is set to be -70 s according to the SNR. The window on positive lag is set to be the same to keep it symmetric. The zero time signals (-20 s to 20 s) are excluded.

A shell script package with database language to use MSNoise can be found at `https://github.com/wwwWeiweiWang/MSnoise1.6_scripts`

Text S2. Testing the relation to water pressure

The velocity variations smoothed by 2-day window are compared to pressure variations (Figure S12) to test if some variations are related to the sea water pressure changes. Six stations, LOBS1, LOBS4, LOBS6, LOBS8, LOBS9, and LOBS10 are equipped with absolute pressure gauges. Pressure data recorded by these LOBSs are 2-day lowpass filtered and averaged. Previous studies (e.g., *King*, 1966) show shear wave velocities increase with hydrostatic pressure. The sea water column puts a hydrostatic pressure on the upper plate. An increase in hydrostatic pressure from the water column change can cause an increase in shear wave velocity. The pressure and dv/v variations are different around SSE2 but are similar before and after SSE2, implying the variations not related to SSE2 might be caused by sea water pressure changes. There is an increase in July 2014 that could conceivably be caused by a sea water pressure change, so we calculate the expected effect of such a water pressure change on velocity.

The biggest pressure increase in July 2014 is about 7 hPa. According to a relationship of shear velocity and effective pressure (*Eberhart-Phillips et al.*, 1989), assuming there is no change on porosity and clay content, shear velocity change caused by pressure change can be written as $\delta Vs = 0.361[(Pe_2 - e^{-16.7Pe_2}) - (Pe_1 - e^{-16.7Pe_1})]$. Here, $Pe_2 - Pe_1 = 7hPa$. Assuming there is no pore fluid pressure change during that time, 7 hPa can cause a shear velocity change of $0.3 \times 10^{-2} m/s$, which is much smaller than the corresponding velocity increase $1380 \times 0.05\% = 0.7 m/s$. Therefore, a change of pressure is too small to cause the observed velocity variation.

Table S1. Final parameters used for MSNoise 1.5.

Parameter	Description	Value
startdate	start date for computation	2014-05-15
enddate	end date for computation	2015-06-23
ref_begin	start date of reference stack	2014-05-15
ref_end	end date of reference stack	2015-06-23
maxlag	maximum lag of cross-correlations	300
cc_sampling_rate	sampling rate for the cross-correlation	20
preprocess_lowpass	preprocessing low-pass filter	2.0 Hz
preprocess_highpass	preprocessing high-pass filter	0.02 Hz
remove_response	remove instrument response	N
corr_duration	data windows to correlate	14400s (LOBSs), 1800s (EOBSs)
overlap	overlap between data windows	0.7
windsorizing	windorizing at N times RMS	3
whitening	whiten Traces before cross-correlation	A (all traces)
stack_method	linear or phase weighted stack	linear
autocorr	compute single station or not	Y
mov_stack	current stack size	20 days
low	the lower frequency bound of whitening	0.05 Hz
high	the upper frequency bound of whitening	0.4 Hz
mwcs_low	the lower frequency bound for MWCS	0.07 Hz
mwcs_high	the upper frequency bound for MWCS	0.4 Hz
mwcs_wlen	window length to perform MWCS	20 s
mwcs_step	step of the moving window in MWCS	4 s
dtt_lag	how the window is defined	static
dtt_minlag	min lag time to compute dtt	20 s
dtt_width	window length to compute dtt	70 s
dtt_sides	which sides of stacks to use	both
dtt_mincoh	threshold of coherence for data	0.89
dtt_maxdt	maximum dt measurement	0.2 s
dtt_maxerr	maximum error on dt measurement	0.1 s

Table S2. Comparison of *Rivet et al.* (2011) and this study.

	dv/v for 2014 Gisborne SSE2	dv/v for 2006 Mexico SSE	dv/v for 2009-2010 Mexico SSE
periods	2.5-6 s	7-17 s	> 12 s
depth	< 7 km (crust in upper plate)	5-20 km (upper and middle crust)	> 10 km (middle and lower crust)
volume change	same order as the estimation using dv/v	much smaller than dv/v	much smaller than dv/v
relate to	strain	strain rate	strain rate

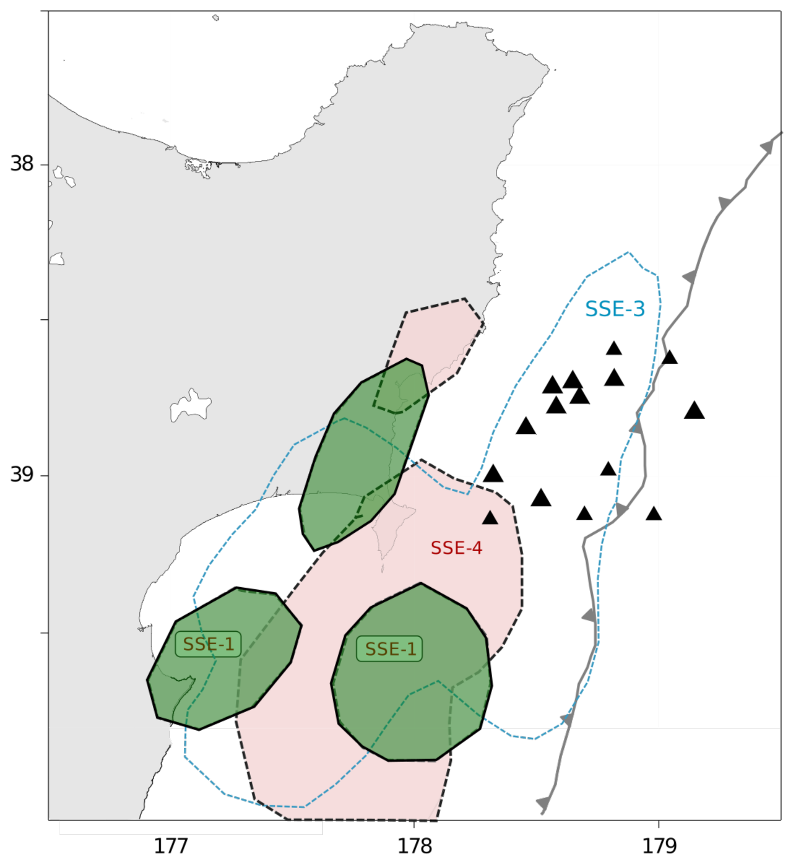

Figure S1. Location of SSE1, SSE3 and SSE4 (*Warren-Smith et al.*, 2019). The green shades mark the regions where SSE1 occurred, the blue dashed line outlines SSE3, and the pink shades mark the location of SSE4.

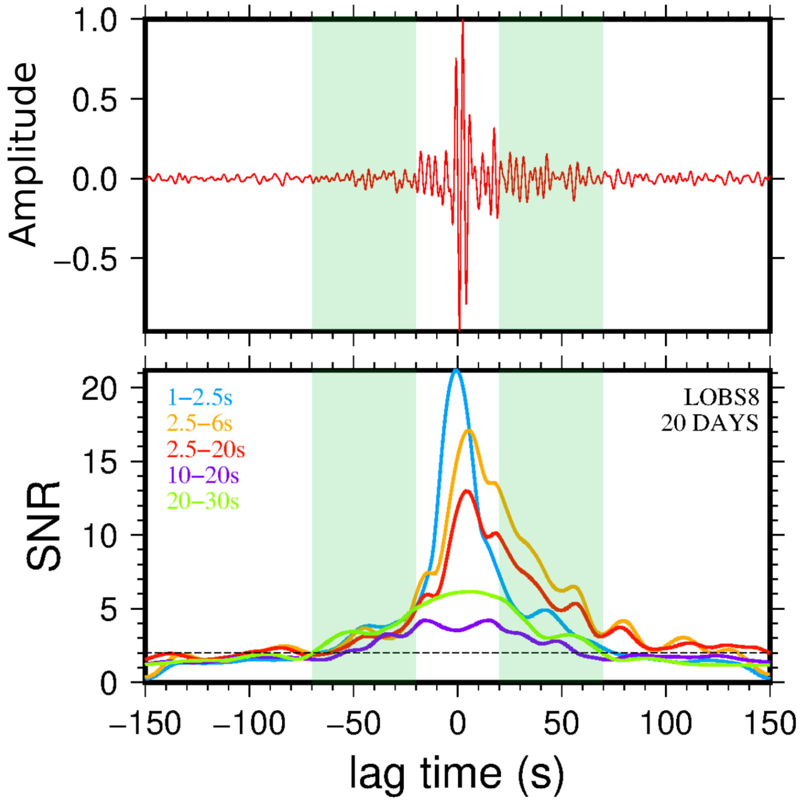

Figure S2. Different filter comparison on LOBS8 vertical-parallel component correlations. A waveform of 20-day stack filtering at 2.5-20 s is shown on the top, which has stronger signal on the positive lag. The amplitude is normalized. The positive lag has stronger signal because the main noise source comes from the ocean side. Lag-time dependent SNRs of different filtered 20-day stacks are computed. The green shades mark the scattered wave window to compute dv/v and the horizontal dashed line in the bottom figure marks SNR=2.

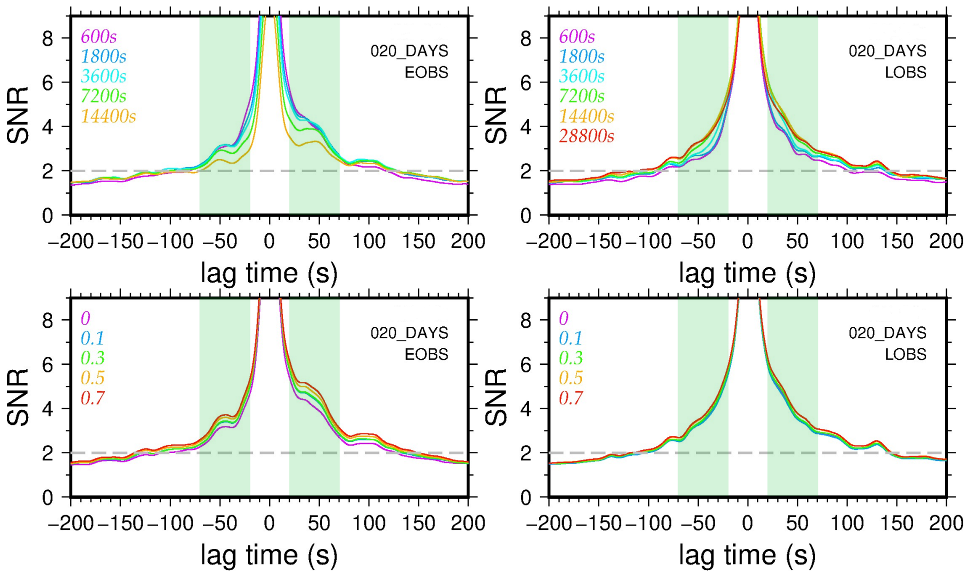

Figure S3. Lag time dependent SNR of different segmentation lengths (upper) and segmentation overlap (bottom). The EOBS SNRs (left) are averaged from different components of the five EOBSs and the LOBS SNRs (right) are averaged from different components of the four LOBSs. The green shades mark the scattered wave window to compute dv/v.

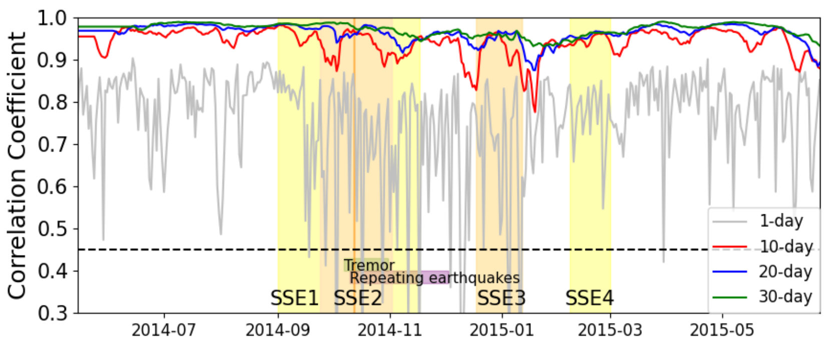

Figure S4. An example of the relationship between stack sizes and correlation coefficients computed on LOBS8 vertical-parallel component correlations. The occurrence of SSEs, tremor and repeating earthquakes are marked. The vertical orange line in SSE2 marks the time when SSE2 finishes its main slip. Correlation coefficients between different size current stacks (1-day stacks, 10-day stacks, 20-day stacks, and 30-day stacks) and reference stack are computed and compared. From 20-day stacks to 30-day stacks, the correlation coefficient is not improved much. The horizontal black dashed line marks the threshold of correlation coefficient=0.45 to exclude daily cross-correlations for LOBS8 vertical-parallel component correlations. For the correlation coefficient threshold of other stations, EOBS1: 0.65; EOBS2: 0.55; EOBS3: 0.55; EOBS4: 0.5; EOBS5: 0.3 for parallel-perpendicular cross-correlations, 0.6 for the other two components; LOBS3: 0.1; LOBS7: 0.45; LOBS9: 0.4.

Figure S5. Available cross component correlations of used stations, after the selection of daily cross-correlations according to the correlation coefficient of the daily cross-correlations and the reference stack. Three colors indicate three different component correlations (Yellow: vertical-parallel; Green: vertical-perpendicular; Blue: parallel-perpendicular). The gap on EOBS5 from the end of 2014 to early 2015 is because of the lack of data. LOBS3 also lost some data from different days, and so the dv/v result from LOBS3 is less reliable. The red rectangle denotes a 20-day window. The daily cross-correlations within the window are stacked to be a current stack.

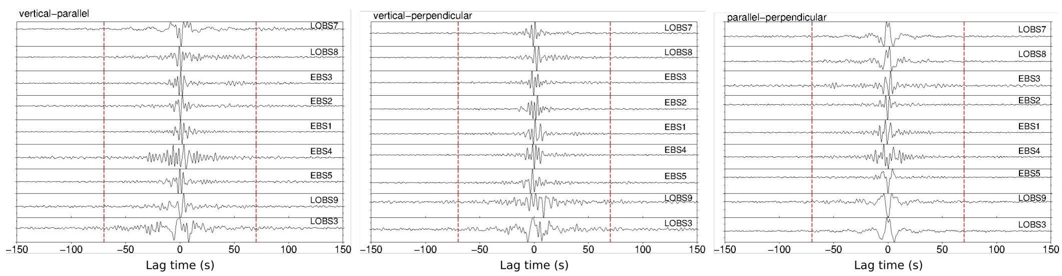

Figure S6. Reference stacks on the three components, plotting from the closest (top) to the furthest (bottom) distance from the coast. Red dashed lines mark the maximum lag times to compute dv/v.

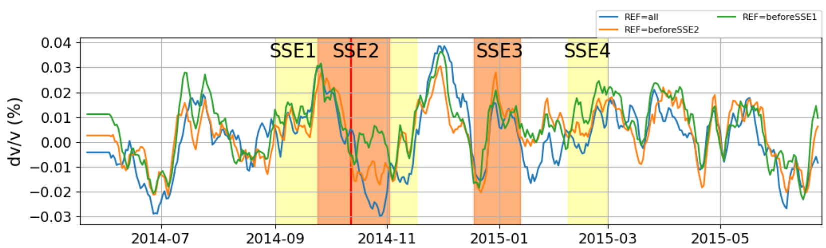

Figure S7. Comparison of velocity variations using a reference stack of all days (blue), before SSE1 (green), and before SSE2 (orange). The four SSEs are marked and the red lines mark the time when SSE2 finishes its main slip.

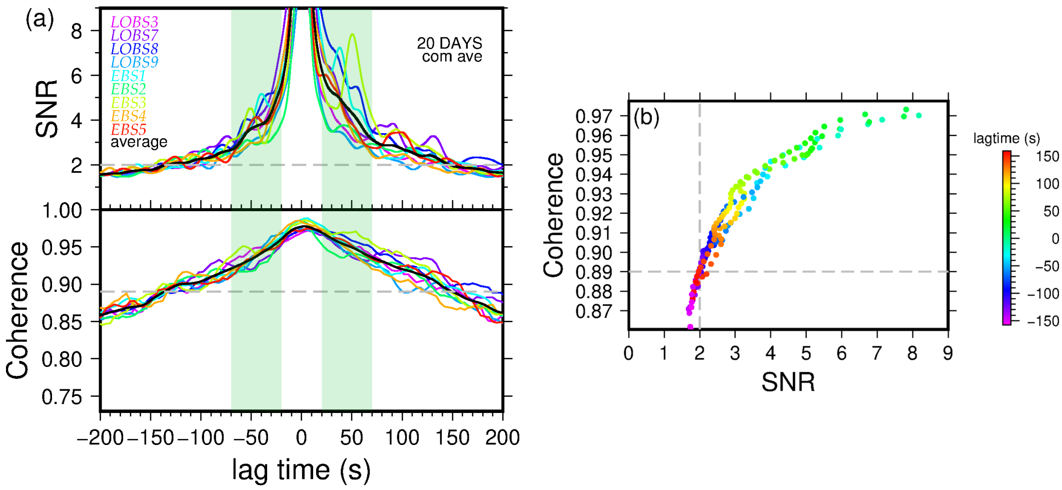

Figure S8. Determination of scattered wave window and threshold of coherence. (a) The final lag-time dependent SNRs and the coherence between current stacks and reference stack of the 20-day current stacks of single stations (color-coded) and their average (black), computed using determined parameters. For each station, the SNR is averaged from its three components. The SNR of each component is averaged from all the 20-day current stacks. The green shades mark the scattered wave window to compute dv/v, which is determined by the SNRs of all single stations above 2. The horizontal dashed line on the top figure marks the threshold of SNR and the one on the bottom figure marks the threshold of coherence. (b) Relationship between the average SNR and coherence (black curves in (a)). The values at different lag times are denoted by different colors. The threshold of coherence is determined by SNR > 2. Thresholds of SNR and coherence are marked by the dashed lines.

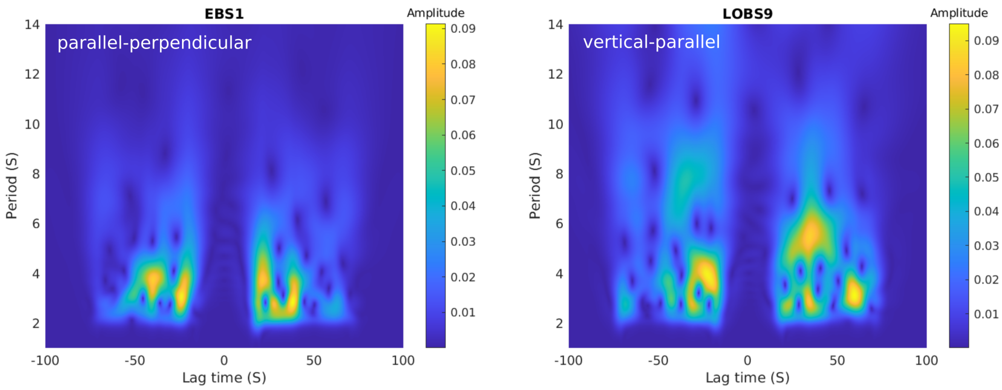

Figure S9. Example spectral analysis on the scattered wave window of the reference stacks. There is no particular period difference between different components, nor is there an obvious difference between broadband LOBSs and short-period EBSs. Some EBSs can reach longer periods (9 s) too.

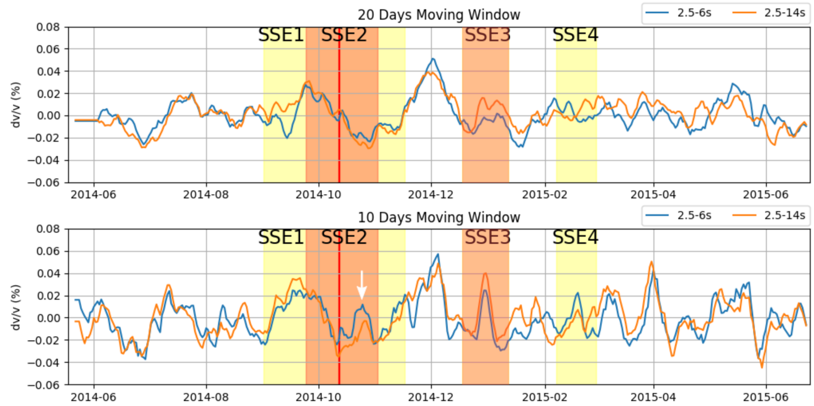

Figure S10. Comparison of dv/v computed at 2.5-6 s (blue) and 2.5-14 s (orange), using 20-day moving window stacks and 10-day moving window stacks. The results at 2.5-6 s are similar to the results at 2.5-14 s. The 10-day moving window dv/v calculation uses less days to stack than 20-day moving window dv/v. Therefore, the 10-day moving window dv/v result is noisier. The velocity decreases caused by SSE2 happen from 24th September to 28th October 2014 in the 20-day moving window result and 20th September to 12th October 2014 in the 10-day moving window result. The velocity increase after the main slip of SSE2 (red line) on 10-day moving window result is indicated by the white arrow. This time difference is because of the time shift from different stack sizes. Although the timing of SSE2 on the 10-day moving window dv/v terminates earlier than that on 20-day moving window dv/v, the velocity decrease on 10-day moving window dv/v happens in the main slip period of SSE2. After the main slip of SSE2, velocity may either increase or decrease.

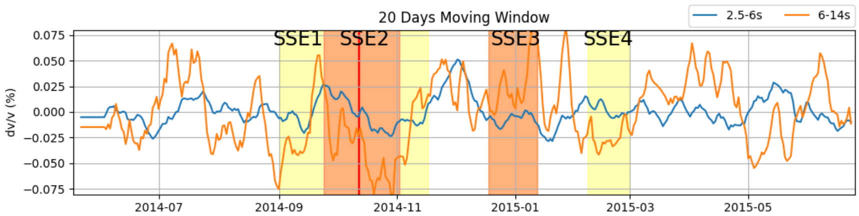

Figure S11. Comparison of dv/v computed at 2.5-6 s (blue) and 6-14 s (orange), using 20-day moving window stacks. The results at 6-14 s are noisy, but still show a velocity decrease during SSE2 and a velocity increase after it.

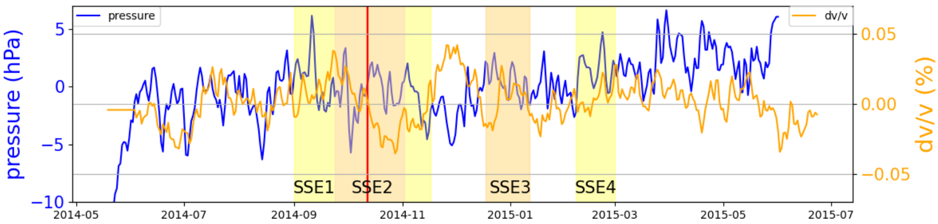

Figure S12. 20-day moving window velocity variations smoothed by 2-day window compared with 2-day low-pass filtered pressure.

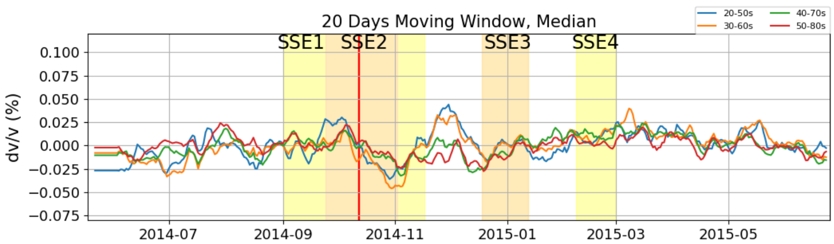

Figure S13. Comparison of velocity variations computed using lag time windows 20-50 s, 30-60 s, 40-70 s, 50-80 s.

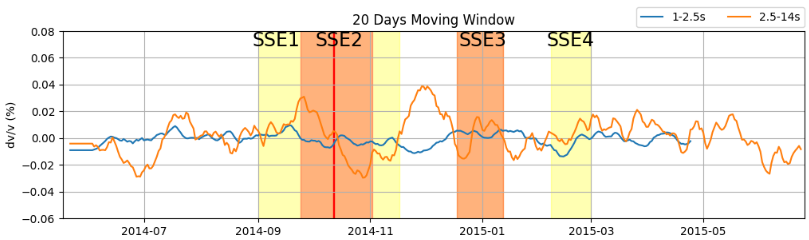

Figure S14. Comparison of velocity variations of 1-2.5 s and 2.5-14 s.

References

Clarke, D., L. Zaccarelli, N. M. Shapiro, and F. Brenguier (2011), Assessment of resolution and accuracy of the Moving Window Cross Spectral technique for monitoring crustal temporal variations using ambient seismic noise, *Geophysical Journal International*, *186*(2), 867–882, doi:10.1111/j.1365-246X.2011.05074.x.

Eberhart-Phillips, D., D.-H. Han, and M. Zoback (1989), Empirical relationships among seismic velocity, effective pressure, porosity, and clay content in sandstone, *Geophysics*, *54*(1), 82–89.

King, M. S. (1966), Wave velocities in rocks as a function of changes in overburden pressure and pore fluid saturants, *Geophysics*, *31*(1), 50–73.

Larose, E., P. Roux, and M. a. Campillo (2007), Reconstruction of Rayleigh–Lamb dispersion spectrum based on noise obtained from an air-jet forcing, *The Journal of the Acoustical Society of America*, *122*(6), 3437–3444, doi:10.1121/1.2799913.

Rivet, D., M. Campillo, N. M. Shapiro, V. Cruz-Atienza, M. Radiguet, N. Cotte, and V. Kostoglodov (2011), Seismic evidence of nonlinear crustal deformation during a large slow slip event in Mexico, *Geophysical Research Letters*, *38*(8), doi:10.1029/2011GL047151.

Warren-Smith, E., B. Fry, L. Wallace, E. Chon, S. A. Henrys, A. F. Sheehan, K. Mochizuki, S. Y. Schwartz, and S. Lebedev (2019), Episodic stress and fluid pressure cycling in subducting oceanic crust during slow slip, *Journal of Geophysical Research: Solid Earth*, doi:10.1038/s41561-019-0367-x.

Yates, A. (2018), Seismic velocity changes at White Island volcano, New Zealand, using ten years of ambient noise interferometry.

Yates, A. S., M. K. Savage, A. D. Jolly, C. Caudron, and I. J. Hamling (2019), Volcanic, Coseismic, and Seasonal Changes Detected at White Island (Whakaari) Volcano, New Zealand, Using Seismic Ambient Noise, *Geophysical Research Letters*, *46*(1), 99–108, doi:10.1029/2018GL080580.